nature communications

Article

https://doi.org/10.1038/s41467-025-60775-5

RFC1 regulates the expansion of neural progenitors in the developing zebrafish cerebellum

Received: 30 July 2024

Accepted: 4 June 2025

Published online: 01 July 2025

Check for updates

Fanny Nobilleau[1,2], Sébastien Audet[1,2], Alexandra da Silva Babinet[1,2], Sanaa Tork[3,4], Charlotte Zaouter[5], Meijiang Liao[1,2], Nicolas Pilon[3,4,6], Martine Tétreault[1,2,4], Shunmoogum A. Patten[1,4,5] & Éric Samarut[1,2,4]

DNA replication and repair are basic yet essential molecular processes for all cells. *RFC1* encodes the largest subunit of the Replication Factor C, an essential clamp-loader for DNA replication and repair. Intronic repeat expansion in *RFC1* has recently been associated with so-called *RFC1*-related disorders, which mainly encompass late-onset cerebellar ataxias. However, the mechanisms making certain tissues more susceptible to defects in these universal pathways remain mysterious. Here, we provide the first investigation of *RFC1* gene function in vivo using zebrafish. We showed that *RFC1* is expressed in neural progenitor cells within the developing cerebellum, where it maintains their genomic integrity during neurogenic maturation. Accordingly, *RFC1* loss-of-function leads to a severe cerebellar phenotype due to impaired neurogenesis of both Purkinje and granule cells. Our data point to a specific role of *RFC1* in the developing cerebellum, paving the way for a better understanding of the pathogenic mechanisms underlying *RFC1*-related disorders.

The cerebellum is the main derivative of the embryonic hindbrain in all vertebrates. It receives and processes information from sensory systems, the spinal cord and other parts of the brain[1–4], using these inputs to ensure that motor movements are smooth, coordinated and efficient[5]. Best known for its motor coordination role, the cerebellum also influences cognitive processes such as attention, language, and modulation of emotional responses[6–8]. Due to all these essential roles, dysfunctions in the development or activity of the cerebellum lead to pathological syndromes associated with movement disorders, problems of balance, posture, and even learning[8–10].

Ataxias are neurodegenerative diseases of the cerebellum and/or brainstem that are characterized by a lack of muscle control or coordination of voluntary movements. These conditions have been linked to hundreds of genes with high phenotypic overlap[11,12]. Particularly, late-onset cerebellar ataxias (LOCA) are a heterogeneous group of cerebellar progressive neurodegenerative diseases that manifest in adulthood with unsteadiness. It is estimated that up to three in 100,000 people worldwide will develop a LOCA. This prevalence is likely underestimated because of the great heterogeneity of clinical presentations, especially in aging patients. The genetic and phenotypic heterogeneity of LOCA contributes to our inability to diagnose ataxia patients, and most LOCA patients remain without a genetic diagnosis[13]. This dampens our understanding of the underlying pathological mechanisms involved in these diseases. However, in 2019, a breakthrough in the genetics of ataxia identified biallelic repeat expansions in the second intron of the *RFC1* gene, encoding Replication Factor C subunit 1. These pentanucleotide repeat expansions are primarily associated with the cerebellar ataxia-neuropathy-vestibular areflexia syndrome (CANVAS)[14,15]. Although it is a rare syndrome, recent findings suggest that *RFC1* expansions are a major cause of a broader

[1]Department of Neuroscience, Faculty of Medicine, Université de Montréal, Montreal, QC, Canada. [2]University of Montréal Hospital Research Center (CRCHUM), Montreal, QC, Canada. [3]Molecular Genetics of Development Laboratory, Département des Sciences Biologiques, Université du Québec à Montréal (UQAM), Montréal, QC, Canada. [4]Centre d'excellence en recherche sur les maladies orphelines – Fondation Courtois (CERMO-FC), Université du Québec à Montréal, Montreal, QC, Canada. [5]INRS- Centre Armand-Frappier Santé Biotechnologie, Laval, QC, Canada. [6]Department of Pediatrics, Faculty of Medicine, Université de Montréal, Montreal, QC, Canada. e-mail: eric.samarut@umontreal.ca

phenotypic spectrum of late-onset progressive ataxias. Moreover, the pathogenic scope of these expansions has been expanded to other movement syndromes, now collectively referred to as *RFC1-related disorders*, which include specific forms of Parkinsonism and multiple systems atrophy (MSA)[16–19]. Although the pathogenicity of *RFC1* repeat expansions is now well established, the underlying mechanisms remain unknown. Recent studies propose that *RFC1* loss-of-function could be at the basis of the repeat expansion pathogenicity[20–23], as the recessive inheritance pattern also suggests. However, other studies showed no specific neurodegenerative phenotype in *RFC1*-depleted neuronal cultures in vitro[24]. This questions the direct involvement of the *RFC1* gene in so-called *RFC1*-related pathologies.

RFC1 encodes the largest subunit of the replication factor C, a DNA-dependent ATPase which loads the DNA-clamp protein PCNA (Proliferating Cell Nuclear Antigen) and recruits DNA polymerases onto DNA undergoing replication or repair[25–27]. The Human Protein Atlas database indicates a ubiquitous tissue expression in adults, which is consistent with its assumed housekeeping function as a DNA repair and replication regulator. Nevertheless, the accurate expression of *RFC1* has not yet been assessed in mammals or vertebrates in vivo, particularly during embryogenesis. Since its cloning in humans in the 90s[28], the function of *RFC1*, particularly in the context of DNA replication and repair, has only been studied in vitro[25,29,30] or in plants[31–33]. Detailed in vivo analysis of its function in animals is needed to better understand *RFC1*-associated diseases.

In this work, we studied the gene and protein expression patterns of *RFC1* in vertebrates, in the developing cerebellum of both mice and zebrafish. This analysis revealed specific expression patterns in neuronal progenitor populations of both Purkinje and granule cell lineages. To circumvent the early embryonic lethality of *Rfc1* knockout mouse models, we generated a zebrafish model of *rfc1* loss-of-function using CRISPR/Cas9 targeted mutagenesis. Although *rfc1*$^{-/-}$ zebrafish larvae die prematurely after 10 days of age, we found that this does not prevent the functional analysis of RFC1 during neurodevelopment. This model uncovered a key role for *rfc1* in the proper development of both granule and Purkinje cell populations. Notably, single-cell transcriptomic approaches showed that *rfc1* regulates the expansion and differentiation of the neuronal progenitor pools. In the absence of *rfc1*, these progenitors accumulate DNA damage and stop proliferating, leading to their death and ultimately severely affecting cerebellum neurogenesis. This specific role of RFC1 during neurodevelopment opens new doors regarding its potential involvement in cerebellar pathologies.

Results

RFC1 is expressed in the developing cerebellum

To evaluate the tissue distribution of *RFC1* in vivo, we first evaluated its mRNA expression in zebrafish embryos via whole-mount in situ hybridization. We found an early broad expression in the developing brain, from 1 day post-fertilization (dpf), with a robust expression in the midbrain-hindbrain boundary (mhb) starting at 2 dpf (Fig. 1A). Using fluorescent in situ RNAscope assays, we showed that at 2 dpf, *rfc1* is expressed on both sides of the midbrain-hindbrain boundary: anteriorly in the developing optic tecum (ot), particularly in the tectal periventricular layer (PVL); posteriorly in the upper rhombic lip (URL), in the forming *valvula cerebelli* (Va) and in the ventral and caudal LRL. We confirmed the identity of these structures using *ptf1a* and *atoh1a* probes as specific markers[34] (Fig. 1B–D and Fig. S1A, B). *Rfc1* diffused expression is sustained in the tectal periventricular layer (PVL) and the developing cerebellar plate *corpus cerebelli* (CCe) from 3 dpf, and its expression overlaps with cerebellar neuronal markers *neurod1* (granule cells) and *pvalb7* (Purkinje cells) (Fig. 1E, F and Fig. S1C, D). Although specific, the expression of *rfc1* in the developing cerebellum is not exclusive especially, at early developmental stages, as an expression signal is also observed in the eye, floor plate and surrounding pharyngeal tissues. To complement these observations at the cellular level and in another vertebrate model, we examined the RFC1 protein distribution in the developing cerebellum of wild-type mice at the cellular level (Fig. 1G–J). Using co-immunolabelling of RFC1 expression with specific markers of Purkinje cells (PC, Calbindin) or granule cells (GC, Pax6), we showed that RFC1 is expressed in early Purkinje cells progenitors (PCp) from P0. Its expression persists in the Purkinje Cell Layer (PCL) at P7, P11, and P60 (Fig. 1G–J, white arrows). Of note is that the nuclear expression of RFC1 in PCp gradually becomes cytoplasmic in more mature PC from P11 onwards. We also found that RFC1 is not expressed in early granule cell progenitors at P0, as shown by the absence of colocalization with the PAX6 marker. However, it is transiently expressed in some migratory granule cells (mGCs) at P11. This stage corresponds to the moment when GCs migrate from the external granule layer (EGL) towards the internal granular layer (IGL), passing through the molecular layer (ML) and the Purkinje cell layer (PCL) (Fig. 1G–J, white arrowheads). Once in the IGL, we could not detect colocalization between RFC1 and the GC marker PAX6. However, we did detect RFC1 expression in some PAX6-positive GCs scattered in the ML. Initially described as ectopic GCs (eGCs), these cells have been recently renamed molecular GCs (mGCs) based on their proven function within the cerebellum circuitry[35]. Altogether, our results show that RFC1 is expressed in the developing cerebellum, both in PC and transiently in a subset of GCs in vertebrates.

Loss of *rfc1* causes survival and morphological anomalies in zebrafish

The Jackson Laboratory Phenotyping Center generated a knock-out (KO) *Rfc1* allele in mice (*Rfc1*$^{tm1b(KOMP)Mbp}$), for which homozygosity was reported to lead to embryonic and/or pre-weaning lethality (no homozygotes over 66 pups at weaning; MGI ID:5495286[36]). In an effort to circumvent this roadblock and with the goal to study the global impact of *RFC1* loss-of-function in vivo in vertebrates, we generated a zebrafish *rfc1* KO model using the CRISPR/Cas9 technology. We targeted the 5th exon and selected a founder line with a 20-bp deletion mutation, which leads to a premature stop codon at position 182 in the zebrafish RFC1 protein (Fig. 2A, B). Of note is that zebrafish have a single *rfc1* ortholog, and it encodes a protein sharing 57% of sequence identity (69% of sequence similarity) with the human RFC1, encompassing the same functional domains (Fig. 2c and Fig. S2). We confirmed *rfc1* loss-of-function at the transcript level both in heterozygous (+/−) and homozygous (−/−) zebrafish larvae (Fig. 2D). Since heterozygous (*rfc1*$^{+/-}$) zebrafish survive to adulthood without overt phenotypes, and retain ~75% of *rfc1* transcript levels (Fig. 2C) compared to wild-type, this suggests that *rfc1* is haplosufficient. In other words, a single functional allele of *rfc1* provides sufficient gene dosage to maintain normal development and survival. However, we found that *rfc1*$^{-/-}$ larvae die prematurely from 8 days of age with no survivors past day 10 ($n = 168$; Fig. 2E). Moreover, *rfc1*$^{-/-}$ larvae depict gross morphological abnormalities from 2 days post-fertilization (dpf). In particular, they display a smaller head, reduced eye diameter and a shorter otic vesicle than their siblings (Figs. S3A, 2B and Fig. 2F–H). These morphological defects become more obvious from 3 dpf and worsen until death. Noteworthy, we did not observe differences in the average body size (Fig. S3B), suggesting that the head morphological phenotype observed in *rfc1*$^{-/-}$ larvae is very specific and not due to developmental delay. Finally, we monitored the swimming behavior of 4 dpf larvae and found that *rfc1*$^{-/-}$ larvae are significantly hypoactive compared to their siblings as assessed by the total distance swum during 60 min (Fig. 2I, J). Altogether, these data show that RFC1 is necessary for normal development, motor behavior and survival in zebrafish. Moreover, its loss-of-function leads to head morphological deformities that we aim to characterize further.

https://doi.org/10.1038/s41467-025-60775-5

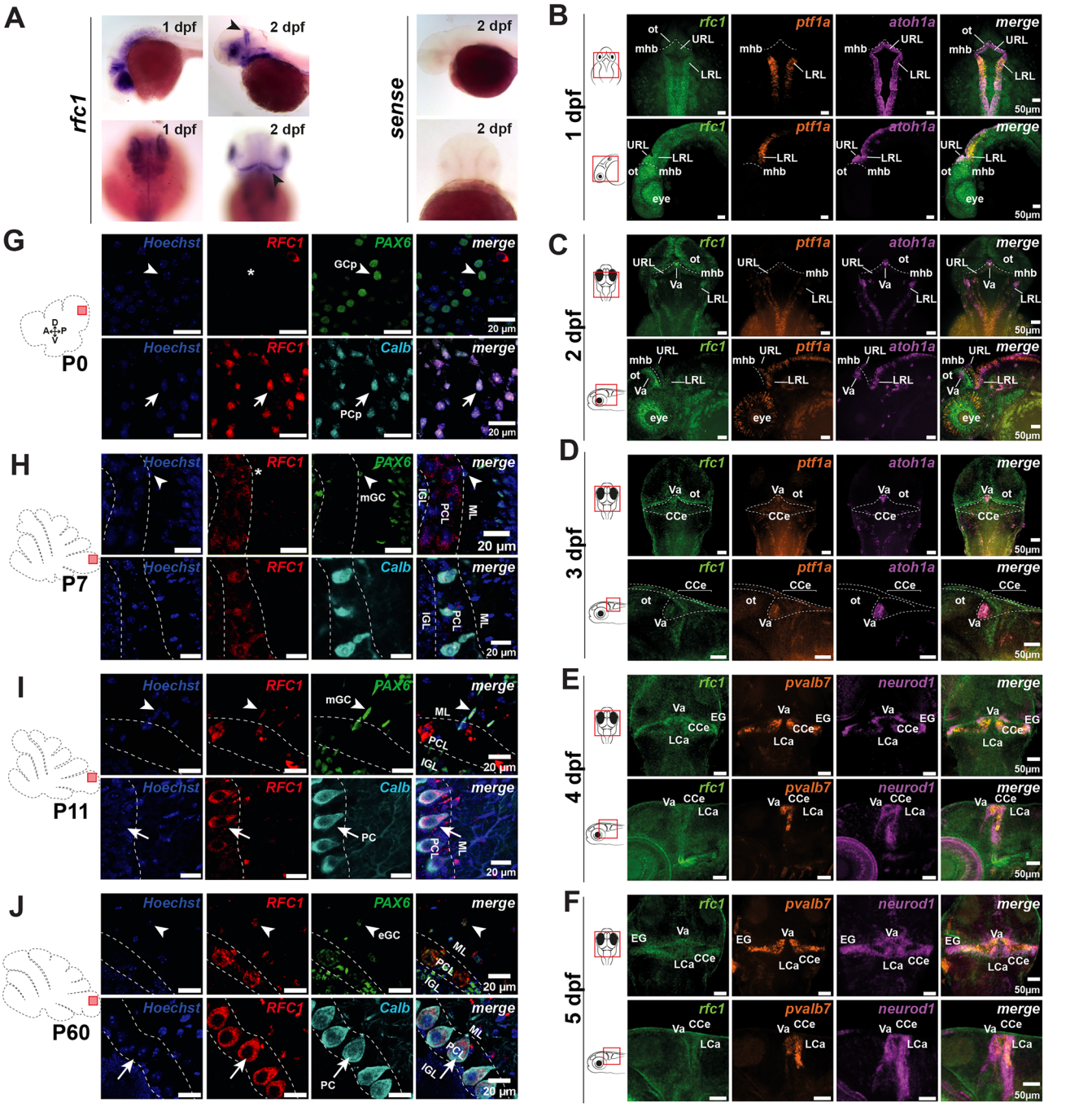

Fig. 1 | *RFC1* is expressed in the developing cerebellum. A Whole-mount in situ hybridization for *rfc1* shows specific, though not exclusive, expression in the developing cerebellum of zebrafish embryos at 1 and 2 days post-fertilization (dpf) (arrowheads; $n \geq 10$ per stage). **B**–**F** RNAscope in situ hybridization detecting *rfc1*, *ptf1a*, and *atoh1a* transcripts at 1 dpf (**B**), 2 dpf (**C**), and 3 dpf (**D**); and *rfc1*, *pvalb7*, and *neurod1* at 4 dpf (**E**) and 5 dpf (**F**). ot optic tectum, mhb midbrain-hindbrain boundary, URL upper rhombic lip, LRL lower rhombic lip, Va *valvula cerebelli*, CCe *corpus cerebelli*, LCa *lobus caudalis cerebelli*; $n = 5$ per stage. **G**–**J** Co-immunofluorescence for RFC1 (red) and either PAX6 (granule cell marker, green) or calbindin (Calb, Purkinje cell marker, green) in the developing mouse cerebellum at postnatal day P0 (**G**), P7 (**H**), P11 (**I**), and P60 (**J**). RFC1 is detected in Purkinje cell progenitors (PCp, arrows in **G**) but absent from granule cell progenitors (GCp, asterisks and arrowheads in **G**). From P11 onwards, RFC1 is observed in some migratory granule cells (mGC, arrowheads in **I**) and in Purkinje cells (PC, arrows in **H**, **I**). At P60 (**J**), RFC1 remains detectable in Purkinje cells (PC, arrows) and in ectopic granule cells located in the molecular layer (eGC, arrowheads). For each stage, images are representative of $N = 3$ animals for P0, P7, and P60, and $N = 4$ animals for P11, with $n = 6$ fields of view per animal. ML molecular layer, PCL Purkinje cell layer, IGL internal granular layer. Scale bars: 50 µm (**B**–**F**), 20 µm (**G**–**J**).

Rfc1$^{-/-}$ zebrafish larvae depict severe cerebellar defects

As we showed that *RFC1* is expressed in the developing brain, particularly at the level of the hindbrain/midbrain boundary, we monitored brain development, particularly the cerebellum, in our *rfc1*$^{-/-}$ zebrafish model. We confirmed that the reduced head size of *rfc1*$^{-/-}$ larvae is accompanied by a general reduction in brain size, particularly at the level of the midbrain as revealed by hematoxylin-eosin staining of brain cross-sections (Fig. 3A). More importantly, unlike in control *rfc1*$^{+/-}$ and wild-type larvae, we were not able to identify any distinct cerebellar structures in 4 dpf *rfc1*$^{-/-}$ larvae cross-sections at the level of the hindbrain (asterisks in Fig. 3A and Fig. S4A). To confirm this observation, we followed by *in toto* immunolabelling the development of the two main

https://doi.org/10.1038/s41467-025-60775-5

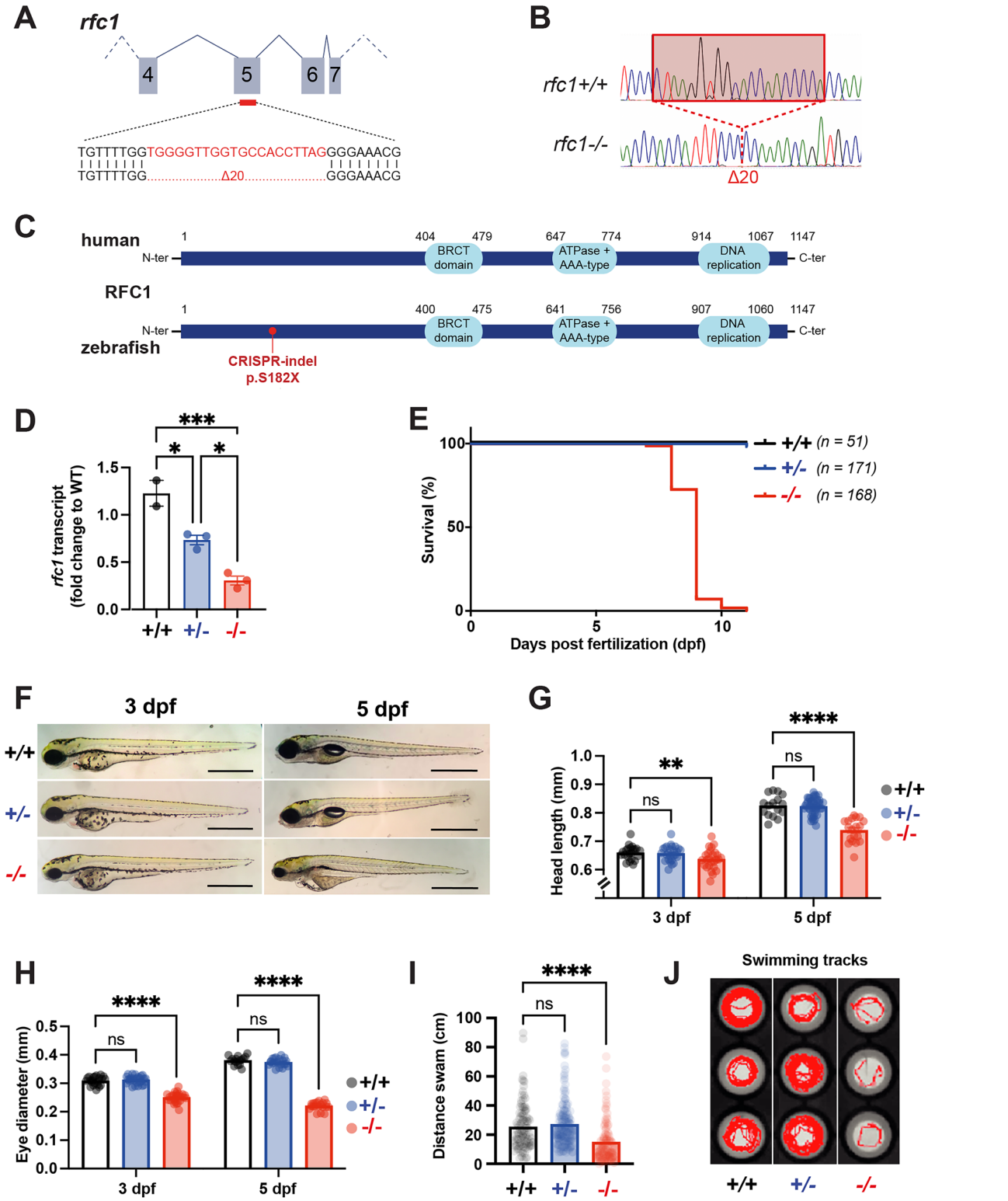

Fig. 2 | *Rfc1* loss-of-function leads to premature death, head morphological anomalies and motility defects in zebrafish. **A**–**C** Generation of an *rfc1* mutant zebrafish line carrying a 20-bp deletion in exon 5, confirmed by Sanger sequencing (**B**). This deletion induces a frameshift resulting in a premature stop codon at position 182 (p.S182X), upstream of all three conserved RFC1 functional domains: BRCT, ATPase+ AAA-type, and DNA replication domains (**C**). **D** RT-qPCR quantification of *rfc1* transcript levels showing a significant reduction in heterozygous ($rfc1^{+/-}$, $n = 3$) and homozygous mutant ($rfc1^{-/-}$, $n = 3$) larvae compared to wild-type ($rfc1^{+/+}$, $n = 2$). **E** Survival curve of zebrafish larvae showing premature lethality of $rfc1^{-/-}$ individuals by 10 days post-fertilization (dpf). **F** Representative images of larvae at 3 and 5 dpf showing reduced head and eye size in $rfc1^{-/-}$ larvae, but not in heterozygous siblings. **G**, **H** Quantification of craniofacial parameters in *rfc1* mutant larvae. **G** Head length at 3 dpf (n = 22 $rfc1^{+/+}$, 26 $rfc1^{+/-}$, 26 $rfc1^{-/-}$) and 5 dpf ($n = 16$ $rfc1^{+/+}$, 41 $rfc1^{+/-}$, 19 $rfc1^{-/-}$). **H** Eye diameter at 3 dpf ($n = 22$ $rfc1^{+/+}$, 28 $rfc1^{+/-}$, 26 $rfc1^{-/-}$) and 5 dpf ($n = 16$ $rfc1^{+/+}$, 22 $rfc1^{+/-}$, 20 $rfc1^{-/-}$). **I** Quantification of total distance swum over 1 h (lights off), demonstrating significant hypomotility in $rfc1^{-/-}$ larvae at 5 dpf compared to siblings ($N = 3$, $n = 101$ $rfc1^{+/+}$, 160 $rfc1^{+/-}$, 107 $rfc1^{-/-}$). **J** Representative swimming tracks recorded over 10 min at 5 dpf, illustrating reduced locomotor activity in $rfc1^{-/-}$ larvae. Data in (**D**, **G**–**I**) are presented as mean ± SEM; individual dots represent biological replicates. Statistical analysis: one-way ANOVA with multiple comparisons. ns not significant ($p > 0.05$); * ($p \le 0.05$); ** ($p \le 0.01$); *** ($p \le 0.001$); **** ($p \le 0.0001$).

https://doi.org/10.1038/s41467-025-60775-5

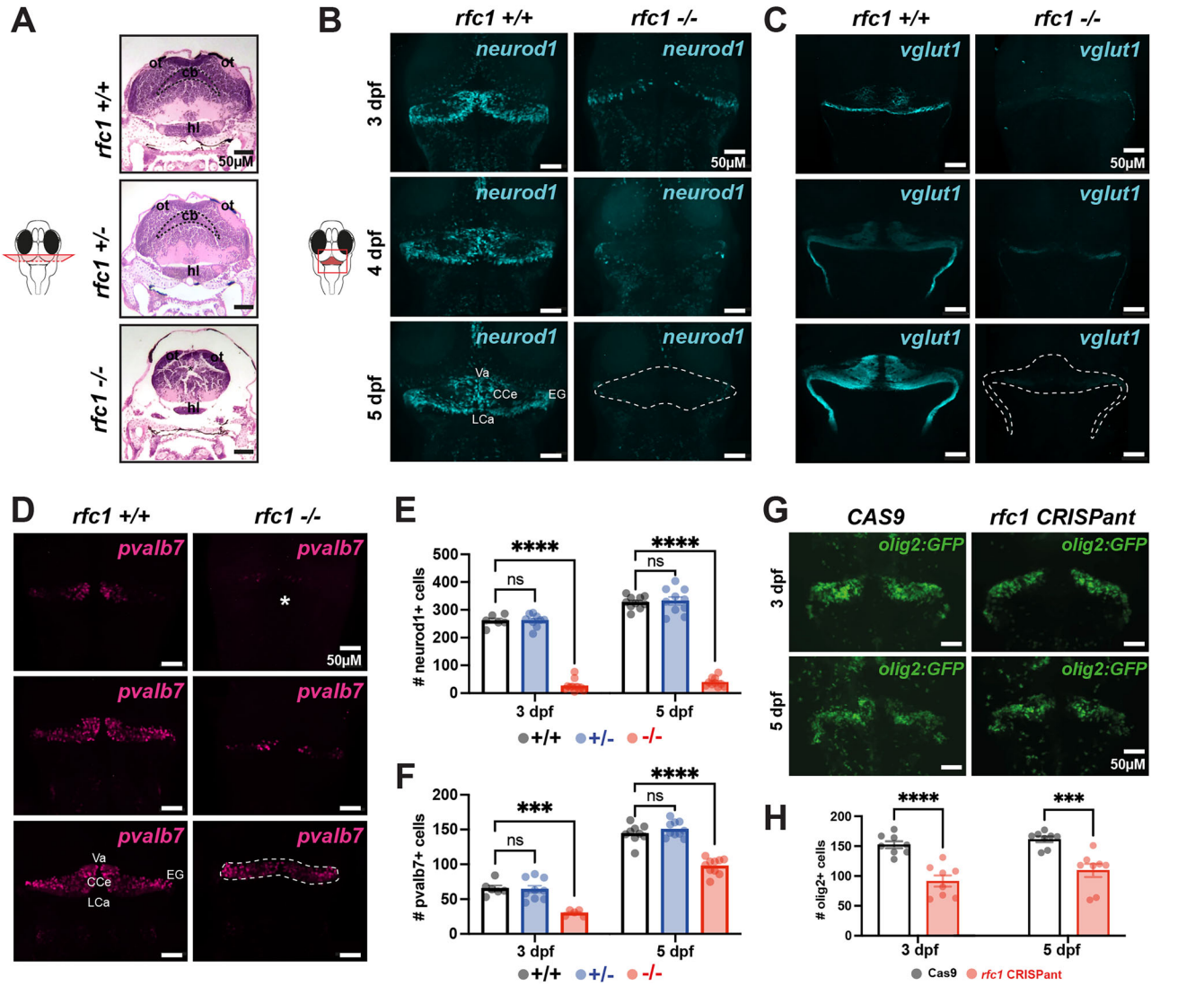

Fig. 3 | *Rfc1*−/− zebrafish larvae exhibit severe cerebellar defects. A Hematoxylin and eosin-stained transverse section of 5 days post-fertilization (dpf) zebrafish larvae at the level of the hindbrain, showing cerebellar hypoplasia in *rfc1*$^{-/-}$ larvae compared to wild-type ($n = 3$) and heterozygous ($n = 5$) siblings. ot optic tectum, cb, cerebellum, hl hypothalamus. **B**–**D** Immunostaining for cerebellar cell types in wild-type and *rfc1*$^{-/-}$ larvae at 3, 4, and 5 dpf. **B** Granule cells labeled with anti-Neurod1 antibody. **C** Granule cell axonal projections labeled with anti-Vglut1 antibody (at 3 dpf $n = 6$ *rfc1*$^{+/+}$, 8 *rfc1*$^{-/-}$; at 4 dpf $n = 5$ *rfc1*$^{+/+}$, 6 *rfc1*$^{-/-}$; and at 5 dpf $n = 7$ *rfc1*$^{+/+}$, *17 rfc1*$^{-/-}$). **D** Purkinje cells labeled with anti-Parvalbumin7 (Pvalb7) antibody. Dotted lines outline the cerebellar structures, highlighting cerebellar loss at 5 dpf in *rfc1*$^{-/-}$ larvae. Asterisks indicate regions of cell loss. **E**, **F** Quantification of Neurod1-positive (**E**, at 3 dpf $N = 2$, $n = 6$ *rfc1*$^{+/+}$, 9 *rfc1*$^{+/-}$, 11 *rfc1*$^{-/-}$ and at 5 dpf $N = 2$, $n = 10$ *rfc1*$^{+/+}$, 10 *rfc1*$^{+/-}$, 10 *rfc1*$^{-/-}$) and Pvalb7-positive (**F**, at 3 dpf $N = 2$, $n = 6$ *rfc1*$^{+/+}$, 9 *rfc1*$^{+/-}$, 5 *rfc1*$^{-/-}$ = 5, and at 5 dpf $N = 2$, $n = 9$ *rfc1*$^{+/+}$, 10 *rfc1*$^{+/-}$, 10 *rfc1*$^{-/-}$) cells at 3 and 5 dpf in *rfc1*$^{+/+}$, *rfc1*$^{+/-}$, and *rfc1*$^{-/-}$ larvae. **G** Confocal imaging of transgenic [*olig2:GFP*] zebrafish larvae injected with Cas9 (control) or CRISPR targeting *rfc1* (CRISPant) at 3 and 5 dpf, showing reduced olig2^{+} cell populations in CRISPants. **H** Quantification of olig2-positive cells in Cas9 and *rfc1* CRISPant larvae ($N = 2$, at 3 dpf $n = 8$ Cas9, 9 *rfc1* CRISPant and at 5 dpf $n = 8$ Cas9, 8 *rfc1* CRISPant). Data in (**E**, **F**, **H**) are presented as mean ± SEM; individual dots represent biological replicates. Statistical analysis: one-way ANOVA with multiple comparisons (**E**, **F**) or unpaired *t*-test (**H**). ns, not significant ($p > 0.05$); * ($p \le 0.05$); ** ($p \le 0.01$); *** ($p \le 0.001$); **** ($p \le 0.0001$). Va valvula cerebelli, CCe corpus cerebelli, LCa lobus caudalis cerebelli, EG eminentia granularis. Scale bars: 50 µm (**A**–**G**).

cerebellar neuronal cell types: Parvalbumin7^{+} PCs and neurod1^{+}/vglut1^{+} GCs (Fig. 3B–F and Figs. S4B, S3C). Consistent with our histological observations, we showed that GCs fail to develop in *rfc1*$^{-/-}$ larvae compared to control siblings (Fig. 3B, C). Indeed, the number of neurod1^{+} GCs is drastically reduced at 3 dpf in *rfc1*$^{-/-}$ larvae (Fig. 3B), also remaining low afterwards (Fig. 3B, E and Figs. S4B, S3C). This is consistent with the absence of vglut1^{+} posterior axonal projections in *rfc1*$^{-/-}$ larvae, which are normally observed from 3 dpf and thicken with age in siblings (Fig. 3C and Fig. S4C). Similarly, albeit less severe, the number of developing parvalbumin7^{+} PCs is significantly reduced in *rfc1*$^{-/-}$ from 3 dpf onwards (Fig. 3D, F and Fig. S4D). Moreover, the general organization of the PC layer is affected in 5 dpf larvae with the absence of the *Valvula cerebelli* structure, a cerebellar structure unique to ray-finned fishes that controls non-locomotor-related functions[37](Fig. 3D and Fig. S3D). To confirm the specificity of these observations, we generated F0-injected *rfc1*-CRISPant larvae targeting each RFC1 functional domain individually (i.e., BRCT, ATPase or DNA replication domain) using specific guide RNAs (Fig. S5A). We showed that all CRISPants phenocopy the small-head and small-eye phenotypes of *rfc1*$^{-/-}$ mutants (Fig. S5B–D), as well as the defects in cerebellar integrity (Fig. S5E, F). Using these F0-CRISPant larvae, we also showed that the integrity of olig2^{+} eurydendroid cells (i.e., the equivalents of the mammalian deep cerebellar nuclei in teleosts[38]) is affected upon *rfc1* loss-of-function (Fig. 3G, H). Overall, these data confirm that *rfc1* is involved in cerebellum development, particularly in populating its neuronal subtypes in vertebrates.

Rfc1 is necessary for early neural progenitor proliferation

To complement our previous observations and in order to dig further into *rfc1*-regulated brain cell populations, we performed deep RNA sequencing of single cells (scRNA-seq) from larval brains *rfc1*$^{-/-}$ and wild-type animals (Fig. 4A). We obtained the single-cell transcriptome of 16140 cells from wildtype and 6583 cells from *rfc1*$^{-/-}$ 4 dpf brains. We processed these data according to the Seurat standard procedure of filtering and clustering to determine cell type identity based on genetic markers of zebrafish brain cell populations at relevant developmental timepoints[39,40].

Consistent with our previous observations, we confirmed the general reduction in the number of cerebellar neuronal clusters defined as PCs (*pvalb7*$^{+}$, *ca8*$^{+}$, *aldoca*$^{+}$, *and ITPR1*$^{+}$) and GCs (*neurod2*$^{+}$, *neurod1*$^{+}$, *zic5*$^{+}$, *FAT2*$^{+}$, *nebl*$^{+}$, *olfm2b*$^{+}$, *cbln12*$^{+}$, and *fabp4b*$^{+}$) in *rfc1*$^{-/-}$ brains (Fig. S6A, 4B). Moreover, we found a significant loss of cell populations constituting clusters identified as neural progenitors (*her4.2*$^{+}$, *her2*$^{+}$, and *sox2*$^{+}$), cycling neural progenitors (*pcna*$^{+}$, *mki67*$^{+}$, and *npm1a*$^{+}$), neuronal progenitors (*dla*$^{+}$, *dlb*$^{+}$, *elavl3*$^{+}$, and *tubb5*$^{+}$) and early neurons (*lhx9*$^{+}$, *elavl3*$^{+}$, and *tubb5*$^{+}$) (Fig. 4B, C and Fig. S6B). Our findings suggest that early processes of neurodevelopment are perturbed in *rfc1*$^{-/-}$ fish.

Given that cerebellar neurogenesis occurs as early as 2 dpf[38,41], we next sought to perform scRNA-seq at 2 dpf. We dissociated the heads of 2-dpf *rfc1*$^{-/-}$ and wild-type larvae and sequenced their individual transcriptomes (18,632 cells from wildtype and 9805 cells from *rfc1*$^{-/-}$, Fig. 4A). Although less severe than at 4 dpf, we noticed a significant reduction in the cellular density of the same clusters defined as neural progenitors, cycling neural progenitors, neuronal progenitors and early neurons (Fig. 4D, E and Fig. S6C).

Consistent with our prior expression analyses during neurodevelopment, we found that *rfc1* is mainly expressed in the neural progenitor and cycling neural progenitor clusters at 4 dpf and 2 dpf, respectively (Fig. S6B, C). Altogether, these observations suggest that RFC1 regulates the development of early neural progenitors, particularly in the developing cerebellum. To confirm this hypothesis, we compared the expression level of specific cerebellar neurogenesis markers[38] *(neurog1, ascl1a*; *atoh1a, atoh1b, atoh1c, zic1, zic4, pax6a for GC neurogenesis*[42,43]; *ptf1a, rorb for PC neurogenesis*[44,45] *and olig2 for eurydendroid cell neurogenesis)*. We found that the expression of these markers is decreased at 3 dpf in *rfc1*$^{-/-}$ larvae compared to their control siblings by RT-qPCR (although not significant for *zic1* and *zic4*) (Fig. 4F and Fig. S7B).

We confirmed this decrease in *rfc1*$^{-/-}$ larval brain by whole-mount in situhybridization and fluorescent RNAscope at 3 dpf (Fig. 4G, H). We also checked the expression of these markers at 2 dpf and 4 dpf and found that while only *atoh1a*, *ptf1a* and *olig2* were significantly reduced in mutants compared to wild-type at 2 dpf, they were all significantly decreased at 4 dpf (Fig. S7A–C). This suggests that these changes caused by the loss of RFC1 arise from 2 dpf with sustained consequences on cerebellar neurogenesis at 3 dpf. Altogether, these results indicate that *RFC1* is expressed in early neural progenitors and is necessary for their neurogenesis, particularly in cerebellar neural progenitors.

RFC1 loss halts cerebellar progenitor proliferation, leading to their death

We next asked what molecular functions are regulated by RFC1 in neural progenitor cells in which it is expressed. To do so, we performed a differential expression analysis on our scRNA-seq datasets at 2 and 4 dpf comparing *rfc1*$^{-/-}$ to wild-type samples (Fig. 5A, B and Supplementary Data 1, 2). Within early progenitor clusters, we found multiple genes involved in early DNA damage response, cell cycle checkpoints, cell proliferation homeostasis, DNA repair and apoptosis to be differentially expressed between *rfc1*$^{-/-}$ and wild-type samples. In particular, we noted the overexpression of early DNA-damage sensor genes in neural progenitor clusters in *rfc1*$^{-/-}$ brains at 2 and 4 dpf (*mdc1*, *atm*, *atr*, *mre11*, and Fanconi anemia complementation group genes (*fancd2* and *fancl*)). These genes are activated in response to DNA damage or replication blockage, and they halt cell cycle progression by controlling critical cell cycle regulators. Particularly, ATM and ATR are thought to be master controllers of cell cycle checkpoint signaling pathways that are required for cell response to DNA damage and genome stability.

Consistently, we noticed an increased expression of many cell cycle checkpoints in the same mutant clusters such as *brca2*, *chek1/2*, *cdk6*, *cdk2*, or *cdkn1a*. Notably, these genes are downstream DNA-damage triggers which stall cell cycle progression. Moreover, several genes involved in the negative regulation of cellular proliferation and cell cycle stalling, such as *nupr1a*, *yap1*, and *btg2*[46–48], were found to be increased in mutant progenitor clusters.

This is consistent with the decrease of proliferation markers such as *cenpf* or *cdca3* in these cell populations. We also found increased expression of multiple genes involved in DNA repair processes, such as *cenpx*, *xpc*, *ercc5/6* and *rpa1/2* (Fig. 5A, B). Those DNA repair and tumor-suppressor genes are activated by cell cycle checkpoint controllers upon alteration in DNA integrity[49–53]. Finally, we showed that the expression of multiple pro-apoptotic genes (*tp53*, *baxa*, *casp8*, *mdm2*, and *mdm4*)[54–57] and *p53* target genes (*rrm2*, *ccng1*, *rps27l*, *sesn1*, and *sesn3*) is increased in these same clusters (Fig. 5A, B). Notably, these gene expression changes are predominant in neural progenitor clusters but also in retinal progenitors at 2 dpf and glia progenitors at 4 dpf.

We wanted to confirm these transcriptomic changes with a series of immunofluorescence labelings *in toto*. To do so, we first immunolabelled embryos using an antibody anti-phosphorylated histone (gH2AX), a marker of DNA damage at the level of the chromatin[58]. We found a significant increase in the number of gH2AX-positive cells in the developing brain of *rfc1*$^{-/-}$ embryos compared to control siblings (Fig. 5C, F, I and Fig. S8A).

Moreover, we assessed cell proliferation using an anti-phosphohistone 3 (PH3) antibody and showed that from 2 dpf, the number of proliferative cells in the developing hindbrain is significantly reduced in *rfc1*$^{-/-}$ embryos (Fig. 5D, G, J and Fig. S8B). Notably, these changes are exacerbated and sustained at 3 dpf in *rfc1*$^{-/-}$ larvae compared to their siblings (Fig. 5E, H, K and Fig. S8C). Finally, when quantifying the number of apoptotic cells at the same stages using an anti-activated caspase-3 antibody, we found a significant increase in the number of dying cells both at 2 and 3 dpf in *rfc1*$^{-/-}$ specifically (Fig. 5E, H).

Interestingly, we do not detect this increase in DNA damage and apoptosis at later stages (4, 5 dpf), reinforcing that RFC1 plays a role during early cerebellar neurogenesis (Fig. S8A–C). We confirmed that these changes occur broadly in the developing brain of *rfc1*$^{-/-}$ embryos, including in the developing cerebellum (Fig. 5F–K). Particularly, by co-labeling cerebellar neural progenitors (*atoh1a* and *ptf1a*) with γH2AX foci, we confirmed that DNA damages accumulate in cerebellar neural progenitors at 2 dpf (Fig. 6A, B and S8D, E).

Finally, we correlated these molecular events (DNA damages and apoptosis) at the level of individual cells within the developing cerebellum, by co-labeling apoptotic DNA fragmentation using TUNEL and gH2AX-positive DNA damage foci in *rfc1*$^{-/-}$ at 2 dpf (Fig. 6C, D, white arrows). Although we could not detect any colocalization of these sparse signals in wild-type brains, we observed overlapping γH2AX and TUNEL signals throughout the midbrain and hindbrain in *rfc1*$^{-/-}$ embryos (Fig. 6C, D).

Additionally, we identified the characteristic γH2AX apoptotic ring pattern, a hallmark of late-stage apoptosis associated with global chromatin fragmentation[59,60]; the latter being the main effector for the apoptotic γH2AX phosphorylation. The presence of this ring, together with apoptotic marker colocalization, and the concomitant reduction in cell proliferation, reinforces that *rfc1*$^{-/-}$ neural progenitor cells

https://doi.org/10.1038/s41467-025-60775-5

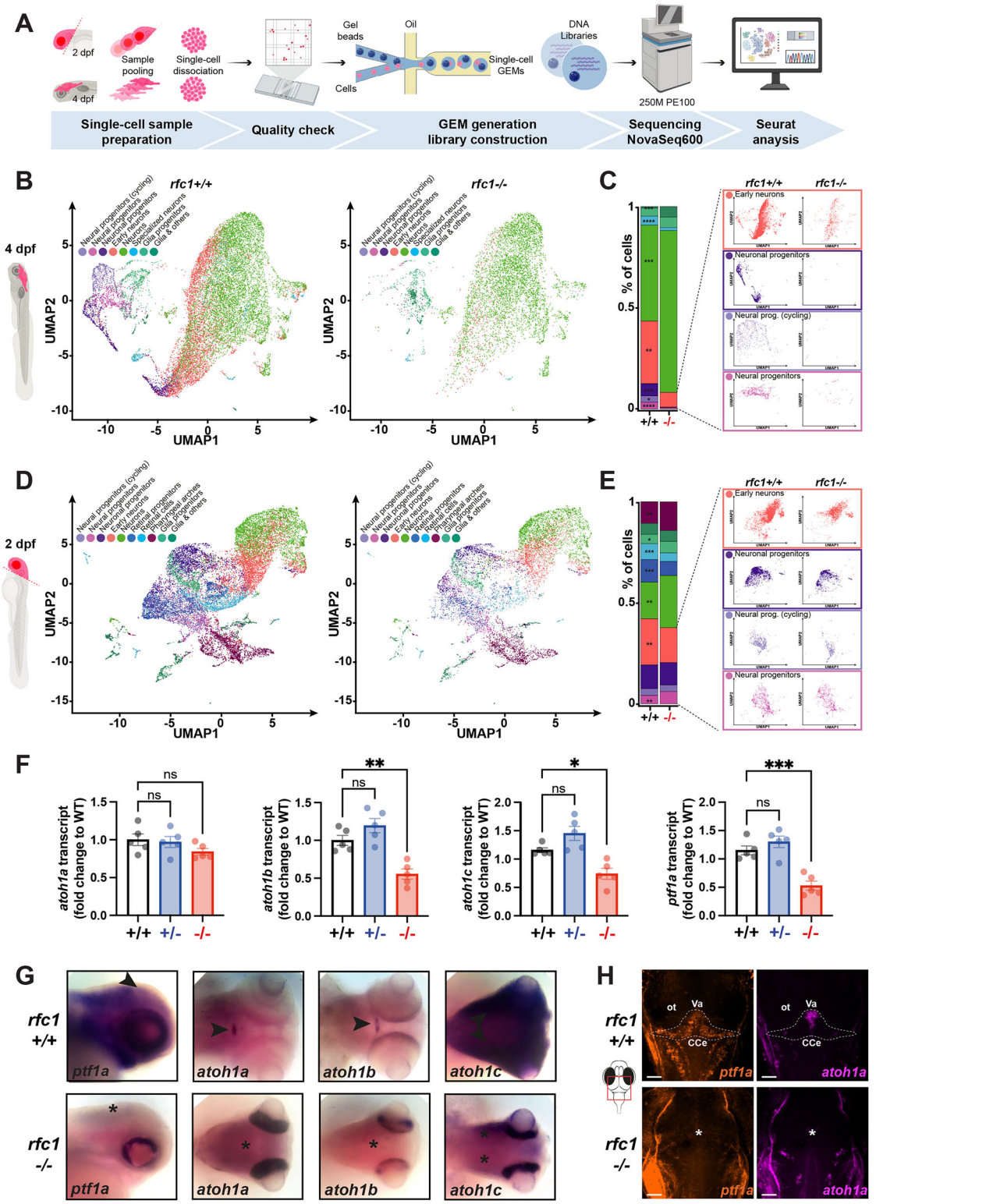

Fig. 4 | *RFC1* is expressed in early neural progenitors and is required for their proliferation. A Workflow for single-cell RNA sequencing (scRNA-seq). Microdissected heads (2 dpf) or brains (4 dpf) from *rfc1*$^{+/+}$ and *rfc1*$^{-/-}$ larvae were pooled (three heads at 2 dpf or four brains at 4 dpf), dissociated, and processed for scRNA-seq using 10X Genomics technology. Created in BioRender. Samarut, E. (2025) https://BioRender.com/k7eukl7. **B**, **D** Uniform manifold approximation and projection (UMAP) plots of scRNA-seq data from 4 dpf (**B**) and 2 dpf (**D**) microdissected brains of *rfc1*$^{+/+}$ and *rfc1*$^{-/-}$ larvae. Clusters of cells have been annotated following Seurat's standard procedure, based on the accumulation of specific genes within top markers (see Supplementary Fig. S5B, C). **C**, **E** Proportions of cells in each identified cluster at 4 dpf (**C**) and 2 dpf (**E**), with UMAPs highlighting clusters significantly reduced in *rfc1*$^{-/-}$ brains. **F** RT-qPCR quantification of *atoh1a*, *atoh1b*, *atoh1c*, and *ptf1a* transcript levels in whole larvae at 3 dpf (*rfc1*$^{+/+}$, *rfc1*$^{+/-}$, and *rfc1*$^{-/-}$, with $n = 5$ for each condition). **G** Whole-mount in situ hybridization for *atoh1a*, *atoh1b*, *atoh1c*, and *ptf1a* transcripts at 3 dpf in *rfc1*$^{+/+}$ and *rfc1*$^{-/-}$ larvae. Expression in the cerebellum of wild-type larvae is indicated by arrowheads; loss of expression in mutants is marked by asterisks. **H** RNAscope in situ hybridization for *ptf1a* and *atoh1a* at 3 dpf in *rfc1*$^{+/+}$ and *rfc1*$^{-/-}$ larvae. Scale bars: 50 µm. ot optic tectum, Va *valvula cerebelli*, CCe *corpus cerebelli*. Data in (**F**) are presented as mean ± SEM; individual dots represent biological replicates. Statistical analysis: one-way ANOVA with multiple comparisons. ns not significant ($p > 0.05$); * ($p \le 0.05$); ** ($p \le 0.01$); *** ($p \le 0.001$); **** ($p \le 0.0001$).

https://doi.org/10.1038/s41467-025-60775-5

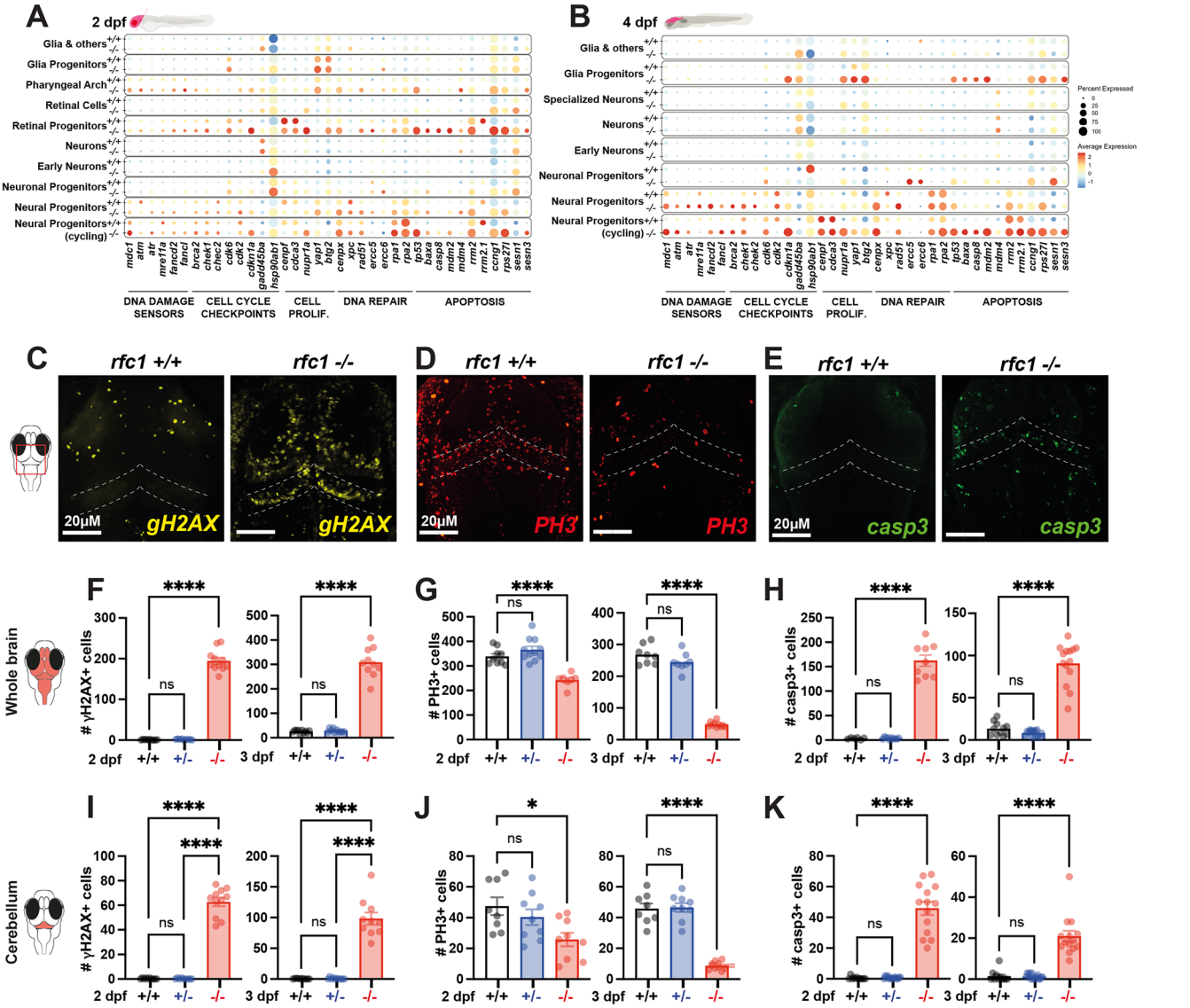

Fig. 5 | RFC1 loss-of-function impairs neural progenitor proliferation and induces cell death. A, B Dot plots showing the expression of genes related to DNA damage sensing, cell cycle checkpoints, proliferation, DNA repair, and apoptosis across individual scRNA-seq clusters at 2 dpf (**A**) and 4 dpf (**B**) in *rfc1*$^{+/+}$ and *rfc1*$^{-/-}$ brains (see Supplementary Fig. S4B, C for cluster annotations). Icons are created in BioRender. Samarut, E. (2025) https://BioRender.com/k7eukl7. **C**–**E** Immunostaining in the developing brain at 3 dpf using: **C** anti-γH2AX antibody (marker of DNA double-strand breaks), **D** anti-phospho-Histone H3 (PH3) antibody (mitotic marker), **E** anti-cleaved caspase-3 (casp3) antibody (apoptosis marker). Dotted lines delineate the developing cerebellum. **F**–**H** Quantification of γH2AX^{+}, PH3^{+}, and caspase-3^{+} cells in the whole brain of *rfc1*$^{+/+}$, *rfc1*$^{+/-}$, and *rfc1*−/− larvae at 2 and 3 dpf. **F** γH2AX-positive cells: 2 dpf (n = 10 *rfc1*$^{+/+}$, 9 *rfc1*$^{+/-}$, 11 *rfc1*$^{-/-}$), 3 dpf (n = 10 *rfc1*$^{+/+}$, 10 *rfc1*$^{+/-}$, 10 *rfc1*$^{-/-}$), N = 2. **G** PH3-positive cells: 2 dpf (n = 9 *rfc1*$^{+/+}$, 11 *rfc1*$^{+/-}$, 7 *rfc1*$^{-/-}$), 3 dpf (n = 8 *rfc1*$^{+/+}$, 8 *rfc1*$^{+/-}$, 8 *rfc1*$^{-/-}$), N = 2. **H** Casp3-positive cells: 2 dpf (n = 6 *rfc1*$^{+/+}$, 10 *rfc1*$^{+/-}$, 9 *rfc1*$^{-/-}$), 3 dpf (n = 11 *rfc1*$^{+/+}$, 15 *rfc1*$^{+/-}$, 14 *rfc1*$^{-/-}$), N = 3. (I–K) Quantification of γH2AX^{+} (**I**), PH3^{+} (**J**), and caspase-3^{+} (**K**) cells in the cerebellum of *rfc1*$^{+/+}$, *rfc1*$^{+/-}$, and *rfc1*$^{-/-}$ larvae at 2 and 3 dpf. **I** γH2AX-positive cells: 2 dpf (n = 10 *rfc1*$^{+/+}$, 10 *rfc1*$^{+/-}$, 11 *rfc1*$^{-/-}$), 3 dpf (n = 10 *rfc1*$^{+/+}$, 10 *rfc1*$^{+/-}$, 10 *rfc1*$^{-/-}$), N = 2. **J** PH3-positive cells cells: 2 dpf (n = 8 *rfc1*$^{+/+}$, 9 *rfc1*$^{+/-}$, 9 *rfc1*$^{-/-}$), 3 dpf (n = 8 *rfc1*$^{+/+}$, 9 *rfc1*$^{+/-}$, 10 *rfc1*$^{-/-}$), N = 2. **K** Casp3-positive cells: 2 and 3 dpf (n = 11 *rfc1*$^{+/+}$, 15 *rfc1*$^{+/-}$, 14 *rfc1*$^{-/-}$), N = 3. Data in (**F**–**K**) are presented as mean ± SEM; individual dots represent biological replicates. Statistical analysis: one-way ANOVA with multiple comparisons. ns not significant ($p > 0.05$); * ($p \leq 0.05$); ** ($p \leq 0.01$); *** ($p \leq 0.001$); **** ($p \leq 0.0001$). Scale bars: 20 µm (**A**–**C**), 1 µm (**D**).

accumulate DNA damages, which trigger the stalling of cell cycle progression and, eventually, programmed cell death.

Discussion

The *RFC1* gene has recently caught attention due to the recent identification of biallelic repeat expansions associated with a wide range of movement disorders, including late-onset cerebellar ataxias such as CANVAS[14,16,17,19]. However, the underlying pathogenic mechanisms were unknown, and this lack of knowledge is largely explained by the fact that the *RFC1* gene function has never been investigated in vivo. Our study is the first to investigate the function of *RFC1* during neurodevelopment, particularly in the cerebellum, the region primarily affected by ataxic cerebellar disorders. We showed that *RFC1* is expressed during cerebellar embryonic development, particularly in expanding neural progenitors in the early zebrafish embryo. Importantly, we showed that the loss of *RFC1* led to a severe cerebellar phenotype characterized by a significant reduction in PCs and GCs and a consistent motor dysfunction.

We unveiled that the loss of *RFC1* jeopardizes the genomic integrity of these progenitor cells, which triggers cell cycle arrest and ultimately leads to their programmed death. Indeed, the spatial and temporal correlation between γH2AX-positive DNA damage

https://doi.org/10.1038/s41467-025-60775-5

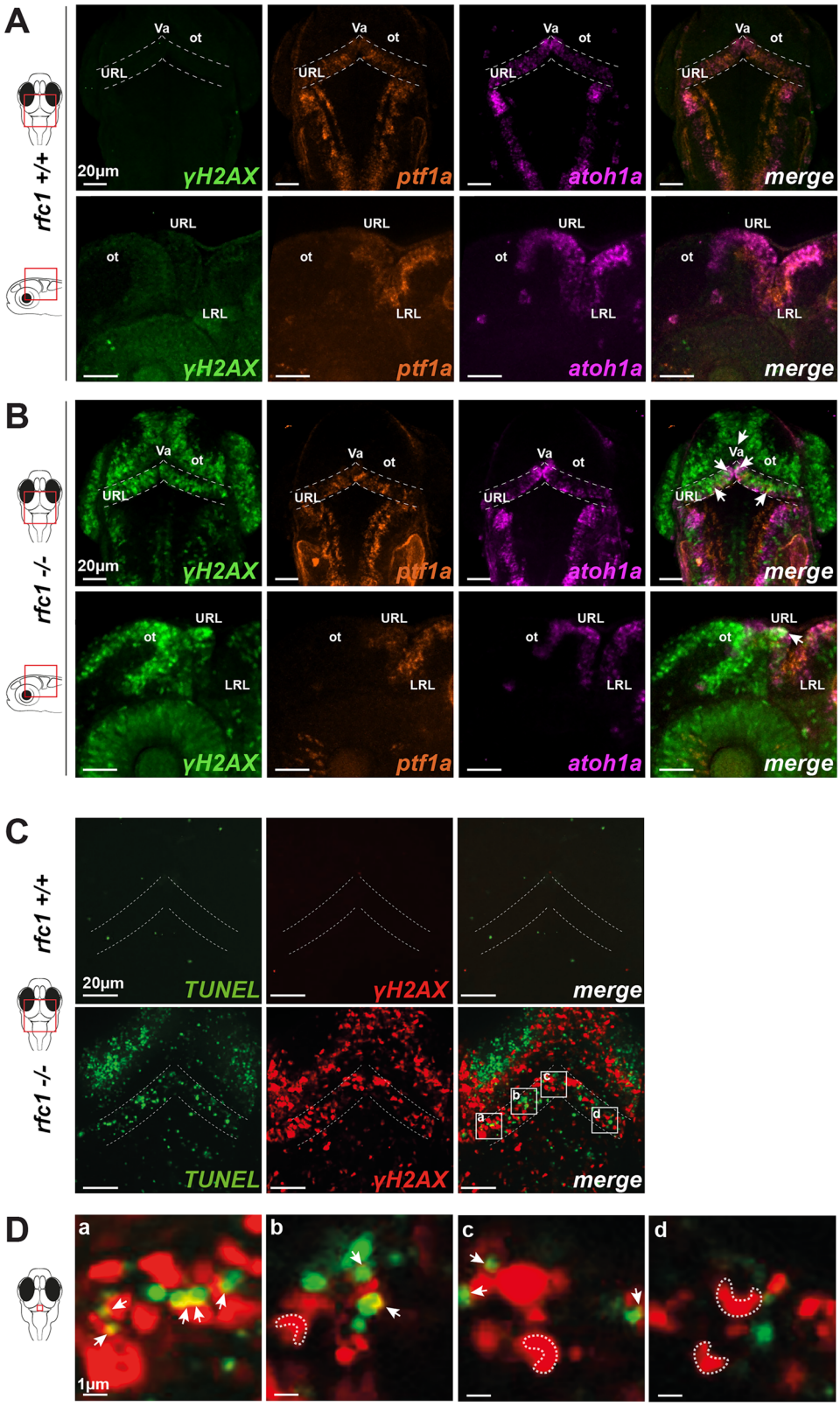

Fig. 6 | Cerebellar neural progenitors accumulate DNA damage and undergo apoptosis in the absence of RFC1. A, **B** Combined immunofluorescence and RNAscope in situ hybridization for DNA damage marker γH2AX (green), *ptf1a* (orange), and *atoh1a* (magenta) at 2 dpf in *rfc1*$^{+/+}$ (**A**, $n = 5$) and *rfc1*$^{-/-}$ (**B**, $n = 5$) embryos. Dorsal views (upper panels) and lateral views (lower panels) are shown. Dotted lines outline the upper rhombic lip (URL). ot optic tectum, LRL lower rhombic lip, Va valvula cerebelli. **C** Confocal images (1-μm optical slice) showing colocalization of apoptotic cells (TUNEL, green) and DNA damage (γH2AX, red) at 2 dpf in *rfc1*$^{+/+}$ ($n = 5$) and *rfc1*$^{-/-}$ ($n = 5$) embryos. Dotted lines delineate the cerebellar region. **D** Higher magnification of selected regions from (**C**) (a–d), highlighting colocalization of TUNEL and γH2AX signals (white arrows) and characteristic γH2AX apoptotic ring patterns (dotted outlines).

accumulation and apoptosis underscores the functional link between DNA damage and cell death fate in the absence of RFC1. Thus, our work is the first to show that *RFC1* plays a crucial role in cerebellar neurogenesis in vivo.

There are multiple DNA repair genes which have been associated with hereditary ataxias: *TDP1* is associated with spinocerebellar ataxia with axonal neuropathy-1 (SCAN1)[61]; *XRCC1* is associated with autosomal recessive cerebellar ataxia[62,63]; *PNKP* is associated with ataxia-oculomotor apraxia-4 (AOA4)[64,65]; *APTX* is associated with ataxia-oculomotor apraxia-1 (AOA1); *PCNA* is associated with ataxia-telangiectasia–like disorder-2 (ATLD2)[66]; *MRE11* is associated with ataxia-telangiectasia–like disorder-1 (ATLD1)[67,68] and *ATM* is associated with ataxia-telangiectasia[69]. The mechanism by which ataxia-associated DNA repair genes lead to preferential cerebellar dysfunction is unknown. It has been suggested that the cerebellum and its main functional components, Purkinje cells, are particularly vulnerable to DNA damage and are therefore more sensitive to changes in these proteins' functions. In this work, we showed that the expression pattern of RFC1 is not ubiquitous during embryo development, as it could have been expected. Moreover, in the postnatal cerebellum, RFC1 expression remains restricted to Purkinje Cells in the cerebellar cortex in mice (Fig. 1G–J).

Thus, this restricted and specific expression pattern could explain how deleterious genetic variations in such universal genes can lead to tissue-specific defects. As a result, instead of explaining the cerebellar-specific effects of these variants by a greater sensitivity of this tissue/cells to DNA damage, it is possible that these genes are expressed in a very specific way at the tissue and cellular level, which explains the specificity of the defects when altered. Because they are involved in late-onset disorders, the mechanisms by which genetic variations in these DNA repair genes, such as RFC1, are mainly speculated in the context of post-mitotic neurons. However, our work suggests that these genes can be specifically expressed in the developing cerebellum and are essential for normal cerebellar neurogenesis. Notably, the investigation of these causative DNA repair genes' function in vivo is hampered by the embryonic lethality of mouse KO models[70]. Our study reveals that it could be insightful to investigate their function in vivo in other vertebrate species, such as zebrafish.

Our data showed that the developing cerebellum is primarily affected by *RFC1* loss-of-function, which is consistent with RFC1's expression pattern in the developing hindbrain. However, it is worth noting that *RFC1* is also expressed in the periventricular layer of the optic tectum as well as in the developing eye, particularly at the level of the ciliary marginal zone. This suggests that it plays a broader role in neurodevelopment, particularly in retinal neurogenesis and explains why the main transcriptomic changes we describe within brain progenitor populations are also found in retinal progenitor cells (Fig. 5A, B). These results are also consistent with the strikingly reduced eye size phenotype observed in *rfc1*$^{-/-}$ larvae compared to their siblings. Although no retinal syndrome has previously been associated with *RFC1* hypomorphism, our data suggest that genetic variants in *RFC1* could be associated with it. However, understanding the mechanisms underlying this phenotype in the eye warrants future studies.

Our results can also be discussed regarding the uncertain pathogenic mechanisms underlying CANVAS. To date, no consensus exists on whether repeated expansions in *RFC1* can cause a gene loss-of-function or a toxic gain of function. Indeed, although truncating variants in *RFC1* have been found in CANVAS patients[20,21] and that in silico analyses suggest repeat-formed secondary DNA structures which could prevent normal transcription[71], no irrefutable evidence of a loss of expression in *RFC1* has yet been provided in post-mortem tissues or in vitro cultures of patient cells. Nevertheless, our data provide evidence that RFC1 is essential for cerebellar development by ensuring genomic integrity during the expansion of neural progenitor populations. Thus, one can speculate that early deleterious changes in RFC1's function or expression during development could affect the proper development of the cerebellum and that these developmental defects could also contribute, at least in part, to the pathogenicity of these repeat expansions. Moreover, it would be interesting to know if structural defects in cerebellar cortical organization could be present before the appearance of symptoms and contribute to the increased sensitivity of the system to DNA damage, for example. This would require generating relevant biological models of the disease, which are complex to mimic, particularly for large repeat expansions.

Finally, our expression data in mice show that *RFC1* is expressed in post-mitotic calbindin-positive Purkinje cells at P60 in a mature cerebellum (Fig. 1J). However, we noticed that RFC1 expression in mature PCs is mainly cytoplasmic. It is, therefore, possible to speculate that *RFC1* might play a distinct role beyond preserving genomic integrity in these post-mitotic neurons. It is worth noting that other DNA replication and repair, protein such as PCNA have been found cytoplasmic with a role in several cellular processes in differentiated cells[72,73].

In sum, our data improve our general knowledge of the in vivo function of the *RFC1* gene and open new avenues of study that may help elucidate the pathogenic mechanisms underlying so-called *RFC1*-related disorders.

Limitations of the study

Late-onset ataxia is, by definition, a disorder occurring at an adult stage. Therefore, our results show that the role of RFC1 during cerebellum neurogenesis cannot be directly transposed to explain the pathogenic mechanisms underlying CANVAS and other late-onset RFC1-related disorders. More work is needed to determine the function of RFC1 in post-mitotic cerebellar neurons, particularly for regulating the maintenance of genomic integrity against DNA damage, against which the cerebellum seems particularly sensitive. Moreover, our functional investigation was carried out on zebrafish, which is a vertebrate. While the cellular organization of the cerebellum has been well conserved from teleosts to mammals, there are some obvious anatomical differences. For instance, the molecular pathways equivalents of the mammalian deep cerebellar nuclei reside in isolated eurydendroid cells (which we show to be affected in *rfc1*$^{-/-}$ larvae, Fig. 3G, H) located within the cerebellar cortex in teleosts[38]. Nevertheless, the molecular pathway regulating its neurogenesis and maturation (including GC internal migration) are well conserved. Moreover, the cerebellum's neuronal cell types, connectivity, and function are highly conserved from teleosts to humans, making the cerebellum one of the highest evolutionary conserved tissues throughout jawed vertebrate brains.

Methods

Experimental models

All experimental procedures involving mice were approved by the institutional ethics committee of the Université du Québec à Montréal (CIPA # 650) in accordance with the biomedical research guidelines of the Canadian Council of Animal Care (CCAC). FVB/N mice initially purchased from Charles River (strain code 207) were maintained and bred in individually ventilated cages within the conventional animal facility of the Université du Québec à Montréal, under 12 h light–12 h dark cycles (7AM to 7PM) at 21.5 °C and 50% humidity and with ad libitum access to regular chow diet (Charles River Rodent Diet #5075, Cargill Animal Nutrition). The brain was collected from newborns, juveniles (postnatal day P7 and P11) and adults (P60) animals of both sexes. Newborns were sacrificed by decapitation, while all P7-P11-P60 mice were sacrificed by transcardiac perfusion with 4% PFA after isoflurane-mediated anesthesia.

Routine zebrafish (*Danio rerio*) maintenance was performed following standard procedures (Westerfield) at 28.5 °C under 12/12 h light/dark cycles at the animal facility of the University of Montreal Hospital Research Center (CRCHUM), Montreal, QC, Canada. All

experiments complied with the guidelines of the Canadian Council for Animal Care. The primary model used for this study was *rfc1* loss-of-function mutants. For generation of the *rfc1* loss-of-function model, zebrafish optimized Cas9 mRNA was synthesized using the mMESSAGE mMACHINE SP6 kit (Ambion) and a pCS2-nCas9n (Addgene #47929) template linearized with NotI. A single-guideRNA sequence (5'-TGGGGTTGGTGCCACCTTAG-3') targeting the 5th exon of *rfc1* was designed using the online tool CRISPRscan and ordered from Synthego, CA, USA. (Tubingen long fin (TL) wild-type embryos were collected for microinjection. A 1nL drop of a mix of 100 ng/μL of Cas9 mRNA and 30 ng/μL of gRNA was injected into one-cell stage embryos using a Picospritzer III pressure ejector. Genotyping of rfc1+/+ (wild-type), +/− (heterozygous) and −/− (homozygous) animals was performed by high-resolution melting analysis (HRM) using genomic DNA extracted by boiling the embryo/larva/clipped caudal fin in 50 mM NaOH for 10 min and then neutralizing it with 100 mM Tris HCl (pH 8). HRM primers were designed using the Universal Probe Library Assay Design Center (Fwd: 5′ GCCATTACTGATGTGGGCATCTG 3′ and Rev: 5′ TGAAAGTCTCCTCCAGCAAATCC 3′). All primer sets are available upon request. The PCR reactions were made with 5 μL of the Precision Melt Supermix for HRM analysis (Bio-Rad #172-5112), 0.5 μL of each primer (10 μM) and 2 μL of genomic DNA and water up to 10 μL. The PCR was performed in a LightCycler 96 Instrument (Roche) using white 96-well plates. The two-step Evagreen PCR reaction protocol was 95 °C for 2 min, then 45 cycles of 95 °C for 10 s and 60 °C for 30 s, followed by 95 °C for 30 s, 60 °C for 60 s, the temperature was increased by 0.02 °C/s until 95 °C for 10 s, then cooling at 40 °C. Curves were analyzed using the Roche LightCycler 96 software. Moreover, polymerase chain reaction (PCR) and sequencing were used to verify the mutation's exact sequence. The following primers were used for genomic PCR: Fwd 5′ TCACGCCTGTAATCCCAGCATTG 3′ and Rev 5′ TCTTGAAGAATAGCTGTGTTGTCCTGTCAC 3′. PCR amplicons were loaded on an agarose gel 1.5% (A87-500G, FroggaBio), and single-band samples were sent to CES Génome Québec (Montréal, Canada) for Sanger sequencing.

To eliminate any putative off-target mutations, the F0 founder was outcrossed with Tubingen long fin wild-type fish for at least three generations before phenotyping the embryos. All experiments were performed on larvae, and the zebrafish sex is not yet determined at this stage. *rfc1*$^{+/-}$ fish were incrossed to obtain *rfc1*+/+, +/−, and −/− from the same cross for experiments. Rfc1+/− fish of different generations have been used to verify the consistency of the phenotype.

Zebrafish morphological analysis

Rfc1$^{+/+}$, $^{+/-}$, and $^{-/-}$ larvae were anesthetized with buffered tricaine methanesulfonate (MS222) and dorsal and lateral images of the whole body were acquired using a 4x magnification under a stereomicroscope (Leica). Body length, eye size, head size and surface area were measured manually using ImageJ software (version 2.3.0). Body length was measured from the anterior tip of the head and the posterior top of the tail. Eye size and otic vesicle diameter or surface area were measured by specifying the eye and vesicle boundaries.

Survival monitoring

About 50 embryos were raised in a dedicated glass beaker, and death was monitored daily. Dead larvae were collected and processed for genomic DNA extraction and high-resolution melting genotyping on the same day. At least two independent batches of larvae were monitored, each containing at least 50 larvae. Data were gathered in GraphPad Prism (version 10) for Kaplan–Meier survival analysis.

Locomotion behavior

At 4 dpf, larvae were separated into single wells of a 96-well plate containing ~200 μL of E3 medium. The plate was placed inside a Daniovision® recording chamber (Noldus). Before the start of the experiment, larvae were habituated for 30 min in the dark. Larval locomotor activity was monitored over 1 h light, 1 h dark cycles over 4 h. The Ethovision XT13 software (Noldus) was used to quantify the total swimming distance per period. Moreover, the swimming tracks were extracted from the integrated view panel of the Ethovision software.

Mouse perfusion and brain cryosection

Mice brains were removed after either head decapitation (P0) or after isoflurane anesthesia and transcardiac perfusion (P7, P11, and P60). Transcardiac perfusion was performed with 1X phosphate-buffered saline (PBS), followed by 4% (w/v) paraformaldehyde solution (PFA). PFA is commonly used to remove blood and preserve the brain for immunostaining. Removed mouse brains were postfixed in 4% PFA solution and left for 24 h at 4 °C. The PFA solution was replaced the next day with a 30% (w/v) sucrose solution (cryoprotection), and the brains were stored at 4 °C until they sank to the bottom of the tube. A cryostat (LEICA CM 1950) was used to slice brain tissues into 10 μm sagittal brain sections (on glass slides) that were kept at −80 °C.

Mouse brain Immunostaining

Brain slices on slides were permeabilized for 2 h in a blocking solution (10 % fetal bovine serum and 1% Triton X-100 in 1X PBS). Sections were then incubated overnight at 4 °C with specific primary antibodies: anti-Calbindin D-28K (cb300, Swant, Switzerland; 1:200) or anti-PAX6 (Biolegend, UK; 1: 200). Subsequently, brain sections were incubated with secondary antibodies, diluted in the same blocking buffer, at room temperature for 2 h. All sections were mounted and counterstained with DAPI (1:1000). A Nikon A1 confocal microscope equipped with NIS-Elements C software (Nikon) was used to acquire images, which were then analyzed using ImageJ.

Zebrafish *in toto* immunofluorescent staining

Larvae were fixed in 4% paraformaldehyde (28908, Thermo Scientific) overnight at 4 °C. The day after, PBS1X-Triton 1% (X-100-500ML, Sigma-Aldrich) was used for several washes over 1 h. Larvae were then incubated in a blocking solution (2% NGS, 1% BSA, 1% DMSO, and PBS1X-Triton 1%) (005-000-121, Jackson Laboratory) for 30 min, and then rinsed several times with PBS1X-Triton 1 %. Larvae were incubated in primary antibodies: anti-pvalb7 (gift from M. Hibi; 1:1000), anti-neurod1 (gift from M. Hibi; 1:500), anti-vglut1 (gift from M. Hibi; 1:1000), anti-gH2AX (GTX127342, GenTex; 1:1000), anti-PH3 (Millipore 09838; 1:500), or anti-cleaved caspase-3 (9661, Cell Signaling; 1:200). The following day, after several washes in PBS1X-Tween 0.1% (P5927, Sigma), larvae were incubated with a secondary antibody diluted in blocking solution: goat anti-mouse Alexa Fluor 488 (A11029, Millipore Sigma; 1:500), goat anti-rabbit Alexa Fluor 488 (A11034, Millipore Sigma; 1:500). For imaging, larvae were positioned in 0.5% low-melting point agarose (16520-050, Thermo Scientific). and acquired using a Zeiss or an Olympus confocal microscope at a 20X or 40X magnification. Images were processed using ZEN (Zeiss) or Volocity (Quorum Technologies) software. Cell counting was performed manually using Image J.

Hematoxylin & Eosin coloration

Briefly, whole 4 dpf larvae or microdissected adult brains were embedded in paraffin and sectioned transversally at 5 μm using Leica microtome (Jung Biocut). The hematoxylin staining was incubated for 4 min, washed with alcohol-acid and rinsed with tap water. Finally, slides were incubated for 10 s in lithium carbonate solution and for 2 min in Eosin staining. Stained samples were mounted under a coverslip using Permount mounting media (3989, Sigma-Aldrich).

Probe cloning and in situ hybridization (RNAscope)

A Specific 504 bp rfc1 probe was cloned from 2 dpf zebrafish cDNAs, using the following primers: Fwd- 5′ TCACGCCTGTAATCCCAGCATTG 3′; Rev- 5′ TCTTGAAGAATAGCTGTGTTGTCCTGTCAC 3′) within the

pCS2+ vector using TOPO TA cloning kit (Invitrogen). Digoxygenin(DIG)-labeled sense and anti-sense RNA probes were in vitro synthesized using the DIG RNA Labeling Kit (Millipore Sigma, Roche-11175033910).

Whole-mount in situ hybridization was performed as described previously[74]. Briefly, larvae were previously fixed in PFA 4% overnight at 4 °C. Embryos were digested with proteinase K (AM2546, Invitrogen): 1 and 2 dpf embryos were incubated at 10 μg/mL for 20 and 30 min, respectively; 3, 4, and 5 dpf larvae were incubated at 20 μg/mL for 30, 35, and 40 min, respectively. After several washes of PBS1X-Tween 0.1%, embryos were fixed with PFA 4% for 20 min. A pre-hybridizing step was performed at 69 °C for 4 h in MH Buffer (50% formaldehyde (FOR001.1, Bioshop), 0.1% Tween, 5X SSC (880-040-LL, Multicell), 11.5 mM citric acid pH6, 50 μg/mL heparin and 500 μg/mL tRNA). DIG probes (11093274910, Sigma-Aldrich) were incubated in MH Buffer at 69 °C overnight. The day after, several washes with a prewarm medium were performed. Then, embryos were blocked for 1–4 h at room temperature in Blocking Buffer (2% sheep serum, 2 mg/ml BSA, PBT). Preabsorbed anti-DIG antibody was added overnight at 4 °C incubation under gentle agitation. On the third day, samples were washed with PBS1X-Tween 0.1% and colored using BCIP/NBT (11681451001, Sigma-Aldrich). Larvae were imaged in 80% glycerol (G5516-1L, Sigma).

RNA extraction and qPCR

RNA was isolated from pools of five larvae using the RNeasy Plus Mini Kit (74134, Qiagen), according to the manufacturer's protocol. Briefly, 500 ng of total RNA was used for cDNA synthesis using the SuperScript®Vilo™ Kit (11754050, Invitrogen).

The cDNA was diluted 1:10 and used for qPCR with SYBR Green I Master (Roche) on a LightCycler 96 instrument. Polr2d and actin B were used as reference genes for normalization. Primers were designed using A plasmid editor (ApE) and span different exons: *rfc1* (Forward) 5′-CCACAGAGAAGAAACACCCAGTAAC-3′ and *rfc1* (Reverse) 5′-GCCGTTCCATTCTCTTTAGGTTTG-3′; *atoh1a* (Forward) 5′-GAGGCGAAGAATGCACGGATTG-3′ and *atoh1a* (Reverse) 5′-TAGTAAGTCGGACAGGGCGTTG-3′; *atoh1b* (Forward) 5′-TGGGAGTAAAGCATCTG TCAGTGG-3′ and *atoh1b* (Reverse) 5′-TCTCCAATGAAGGAATGACGC TTCTC-3′; *atoh1c* (Forward) 5′-GCTAACGCCCGAGAGAGGAG-3′ and *atoh1c* (Reverse) 5′- TCTGTGCCATCTGAAGCGTCTC-3′; *ptf1a* (Forward) 5′-CCACACAGTGACGCCTTAAACC-3′ and *ptf1a* (Reverse) 5′-GAGAGTGTCCTGCGAGAGGAG-3′; *polr2d* (Forward) 5′-AACGCAAAG TGGGAGATGTG-3′ and *polr2d* (Reverse) 5′-AGCGTCTCTGCGTTCTCAA-3′); *actinb* (Forward) 5′-CCAGCTTTTCAGCCTCACTT-3′ and *actinb* (Reverse) 5′-CGGCAATTTCATCATCCAT-3′. The $2^{-\Delta\Delta CT}$ algorithm was used to *analyze* the relative changes in gene expression between samples.

Single-cell dissociation

Larval brains were microdissected from 4 dpf pre-genotyped larvae using fine forceps in calcium-free Ringers' solution. For 2 dpf embryos, heads were cut off using sharp microblades. A total of four brains or three heads were pooled per sample and transferred into a 1.5 ml tube containing 250 μl of dissociation solution containing 0.02% papain (LS003124, Worthington), 0.02% DNase I (LK003170, Worthington), and 12 mg/ml L-cysteine into 5 mL of DMEM/F12 (11320-033, Gibco). Tissues were digested at 37 °C for 10 min and slowly pipetted up and down ten times, then incubated for an additional 10 min followed by pipetting up and down 10–13 times. To stop the enzymatic digestion, 1 ml of washing solution (30% glucose, 0.5% HEPES (15630-080, Gibco), and 5% FBS in DPBS 1X (14040-141, Gibco)) was added. Samples were then centrifuged at 4 °C at 800×*g* for 5 min. The supernatant was discarded and 50 μl of washing solution was added to resuspend the pellet. The cell suspension is filtered out with a cell strainer (136800040, SP Bel-Art, Wayne, USA) to remove aggregates or duplets. Single-cell suspension and cell number was assessed on a Kova slide, and cell mortality was assessed using Trypan blue. Fresh single-cell samples were sent to the Montreal Clinical Research Institute (IRCM) genomic platform. Libraries were prepared using the Chromium Single Cell 3′ reagent kits. Reads obtained from the 10X Genomics platform were processed using the 10X Genomics Cell Ranger v7.1.0 pipeline and Cloud Analysis[75], which includes STAR v2.7.2a alignment[76] against the Danio Rerio GRCz11 genome with the corresponding Ensembl annotations (release 110)[77].

Single-cell data analysis

The bioinformatics analysis was performed in R (v4.3.1) using packages centered around Seurat v5.0.0[78]. Quality control steps included cell scoring with PercentageFeatureSet for mitochondrial genes (^mt-), ribosomal genes (^rp[sl]), and hemoglobin genes (^hba.*$|^hbb.*$). Cells were removed when they had poor sequencing depth (features ≤300; counts ≤500), abnormally high mitochondrial content (≥20%)[79], or significant hemoglobin content (≥1%). Potential multiplets were removed by filtering out cells with outlier sequencing depth (features ≥6000; counts ≥50,000). Features not present in at least three cells were also excluded from the analysis.

The Seurat RNA assay data were then log-normalized with NormalizeData default parameters, and scaled across all remaining genes. Additionally, an SCT assay was generated using SCTransform (vst.flavor = v2), and mitochondrial content was regressed during the gene expression transformation (vars.to.regress)[80].

Clustering, annotations, and population composition analysis

Dimensionality reduction calculations, such as the principal component analysis (PCA) and subsequent uniform manifold approximation and projection (UMAP), were utilized in the SCT assay. The appropriate number of dimensions for the initial clustering was determined using a combination of ElbowPlot and Jackstraw functions to assess the significance of the top 50 principal components[81].

The FindMarkers function identified differentially expressed genes within each resulting cluster, which served to assess cell identities. Cell type annotations were curated manually by comparing top markers to annotations databases such as Daniocell and Zebrahub[40,82]. Subclustering was conducted to ensure cluster identity was not driven by small populations of specialized cells. Cell types were also validated by projecting online annotations onto the cells to observe correlating results[38]. While top markers of each presented cluster can be visualized through dot plots (Fig. S4B, C), more extensive marker lists are available (Supplementary Data 1, 2). Markers that define cell identity are provided for 2 dpf and 4 dpf with a cutoff of log fold change >0.5, and a minimum percentage of expression across cells of 0.2.

Determination of differential cell population abundance between conditions was computed using the DCATS v0.99.6 beta-binomial generalized linear statistical model to compare annotated clusters[83]. Cell ratio bar plots utilized the DittoSeq v1.12.2 package[84]. Subsequently, the FindMarkers function (logfc.threshold = 0.5; min.pct = 0.2) was employed to identify differentially expressed genes associated with significantly altered cell types between wild type and knock-out samples.

Imaging

Imaging was performed using either a Zeiss Axio Observer.Z1 equipped with a Yokogawa CSU-X1 spinning disk confocal module (Zeiss, Germany) and a motorized stage (ASI system with an MCL nano-drive piezo for precise focus control) or an Olympus confocal microscope. For spinning disk confocal imaging, images were acquired using ZEN 2.6 (Blue Edition) software (version 2.6.76.00000). Excitation was provided by a diode laser at 488 nm, controlled by acousto-optic tunable filters (AOTF), and emission was optimized for Alexa Fluor 488 using filters designed for a peak emission around 517 nm (DBP 527/

54 + 645/60 from Chroma). Detection was performed using an EMCCD Evolve 512 monochrome camera (Photometrics) (Photometrics, PvCamEvolve_512) with a native pixel size of 16 μm, a 512 × 512 resolution, 16-bit depth, and a 1.2x EMCCD camera adapter. A Plan-Apochromat 20×/0.8 M27 objective (Zeiss, Germany) was used, with a physical pixel size of 0.67 × 0.67 μm in the XY plane. Z-stacks were acquired with an interval of 0.54 μm. Tiling was used to acquire larger fields of view, and the images were stitched using the ZEN 2.6 (blue edition) Tiling module, ensuring seamless reconstruction of the larger areas with 10% overlap. Post-acquisition image processing was carried out using ImageJ or Volocity (Quorum Technologies). Manual cell counting was performed with ImageJ/FIJI. Brightness and contrast adjustments were applied uniformly across datasets to enhance image clarity while preserving data integrity.

Quantification and statistical analysis

Morphological and locomotion parameters were quantified using DanioScope and EthoVision software (Noldus) as described above. All data acquisition and analyses were performed by experimenters blinded to the genotype of the larvae. For all experiments, "*N*" refers to the number of independent biological replicates (i.e., distinct batches of embryos), and "*n*" refers to the number of individual larvae analyzed per condition. Each experiment was independently repeated at least twice. Before conducting parametric tests, data were tested for normality using the Shapiro–Wilk test. When data met the assumptions of normality, an unpaired Student's *t*-test (for two-group comparisons) or a one-way analysis of variance (ANOVA) (for comparisons among more than two groups) was performed. When ANOVA revealed a significant effect, Tukey's post hoc test was used for multiple comparisons. The exact statistical test used for each analysis is now indicated in the corresponding figure legends. All statistical analyses and graphs were generated using GraphPad Prism software. Data were expressed as mean ± standard error of the mean (SEM). Significance thresholds were set as follows: ns ($p > 0.05$); * ($p \leq 0.05$); ** ($p \leq 0.01$); *** ($p \leq 0.001$); **** ($p \leq 0.0001$).

Reporting summary

Further information on research design is available in the Nature Portfolio Reporting Summary linked to this article.

Data availability

Single-cell RNA-seq data have been deposited in the NCBI BioProject PRJNA1126282 and are publicly available as of the date of publication. Original in situ hybridization images and microscopy data reported in this paper can be shared by the lead contact upon request. The rfc1-KO zebrafish line generated in this study is cryopreserved at the University of Montreal Hospital Research Center (CRCHUM) and is available upon request and signature of a Material Transfer Agreement between the CRCHUM and the requestor. Further information and requests for resources and reagents should be directed to and will be fulfilled by the lead contact, Dr. Éric Samarut (eric.samarut@umontreal.ca). Source data are provided with this paper.

Code availability

All original code have been deposited and made publicly available on Zenodo as of the date of publication. (https://doi.org/10.5281/zenodo.15499729). Any additional information required to reanalyze the data reported in this paper is available from the lead contact upon request.

References

1. Voogd, J. The human cerebellum. *J. Chem. Neuroanat.* **26**, 243–252 (2003).
2. Purves, D. et al. *Circuits within the Cerebellum* (Sinauer Associates, 2001).
3. Fine, E. J., Ionita, C. C. & Lohr, L. The history of the development of the cerebellar examination. *Semin. Neurol.* **22**, 375–384 (2002).
4. Roostaei, T., Nazeri, A., Sahraian, M. A. & Minagar, A. The human cerebellum: a review of physiologic neuroanatomy. *Neurol. Clin.* **32**, 859–869 (2014).
5. Manto, M. et al. Consensus paper: roles of the cerebellum in motor control-the diversity of ideas on cerebellar involvement in movement. *Cerebellum* **11**, 457–487 (2012).
6. Kim, L. H., Heck, D. H. & Sillitoe, R. V. Cerebellar functions beyond movement and learning. *Ann. Rev. Neurosci.* 47, 145–166 (2024).
7. Koziol, L. F. et al. Consensus paper: the cerebellum's role in movement and cognition. *Cerebellum* **13**, 151–177 (2014).
8. Strick, P. L., Dum, R. P. & Fiez, J. A. Cerebellum and nonmotor function. *Annu. Rev. Neurosci.* **32**, 413–434 (2009).
9. Schmahmann, J. D. Disorders of the cerebellum: ataxia, dysmetria of thought, and the cerebellar cognitive affective syndrome. *J. Neuropsychiatry Clin. Neurosci.* **16**, 367–378 (2004).
10. Bodranghien, F. et al. Consensus paper: revisiting the symptoms and signs of cerebellar syndrome. *Cerebellum* **15**, 369–391 (2016).
11. Tsang, H., Addepalli, K. & Davis, S. R. Resources for interpreting variants in precision genomic oncology applications. *Front. Oncol.* **7**, 214 (2017).
12. Ngo, K. J. et al. A diagnostic ceiling for exome sequencing in cerebellar ataxia and related neurological disorders. *Hum. Mutat.* **41**, 487–501 (2020).
13. van Gaalen, J. & van de Warrenburg, B. P. A practical approach to late-onset cerebellar ataxia: putting the disorder with lack of order into order. *Pr. Neurol.* **12**, 14–24 (2012).
14. Cortese, A. et al. Biallelic expansion of an intronic repeat in RFC1 is a common cause of late-onset ataxia. *Nat. Genet.* **51**, 649–658 (2019).
15. Rafehi, H. et al. Bioinformatics-based identification of expanded repeats: a non-reference intronic pentamer expansion in RFC1 causes CANVAS. *Am. J. Hum. Genet.* **105**, 151–165 (2019).
16. Sullivan, R. et al. RFC1-related ataxia is a mimic of early multiple system atrophy. *J. Neurol. Neurosurg. Psychiatry* **92**, 444–446 (2021).
17. Ylikotila, P. et al. Association of biallelic RFC1 expansion with early-onset Parkinson's disease. *Eur. J. Neurol.* **30**, 1256–1261 (2023).
18. Malaquias, M. J. et al. Multisystemic RFC1-related disorder: expanding the phenotype beyond cerebellar ataxia, neuropathy, and vestibular areflexia syndrome. *Neurol. Clin. Pr.* **13**, e200190 (2023).
19. Davies, K., Szmulewicz, D. J., Corben, L. A., Delatycki, M. & Lockhart, P. J. RFC1-related disease: molecular and clinical insights. *Neurol. Genet.* **8**, e200016 (2022).
20. Benkirane, M. et al. RFC1 nonsense and frameshift variants cause CANVAS: clues for an unsolved pathophysiology. *Brain* **145**, 3770–3775 (2022).
21. Ronco, R. et al. Truncating variants in RFC1 in cerebellar ataxia, neuropathy, and vestibular areflexia syndrome. *Neurology* **100**, e543–e554 (2023).
22. Arteche-Lopez, A. et al. New cerebellar ataxia, neuropathy, vestibular areflexia syndrome cases are caused by the presence of a nonsense variant in compound heterozygosity with the pathogenic repeat expansion in the RFC1 gene. *Clin. Genet.* **103**, 236–241 (2023).
23. Abdi, M. H., Zamiri, B., Pazuki, G., Sardari, S. & Pearson, C. E. Pathogenic CANVAS-causing but not non-pathogenic RFC1 DNA/RNA repeat motifs form quadruplex or triplex structures. *J. Biol. Chem.* https://doi.org/10.1016/j.jbc.2023.105202 (2023).
24. Maltby, C. J. et al. AAGGG repeat expansions trigger RFC1-independent synaptic dysregulation in human CANVAS neurons. *Sci. Adv.* **10**, eadn2321 (2024).
25. Zhang, G., Gibbs, E., Kelman, Z., O'Donnell, M. & Hurwitz, J. Studies on the interactions between human replication factor C and human

proliferating cell nuclear antigen. *Proc. Natl Acad. Sci. USA* **96**, 1869–1874 (1999).
26. Bowman, G. D., O'Donnell, M. & Kuriyan, J. Structural analysis of a eukaryotic sliding DNA clamp-clamp loader complex. *Nature* **429**, 724–730 (2004).
27. Zhuang, Z., Yoder, B. L., Burgers, P. M. & Benkovic, S. J. The structure of a ring-opened proliferating cell nuclear antigen-replication factor C complex revealed by fluorescence energy transfer. *Proc. Natl Acad. Sci. USA* **103**, 2546–2551 (2006).
28. Bunz, F., Kobayashi, R. & Stillman, B. cDNAs encoding the large subunit of human replication factor C. *Proc. Natl Acad. Sci. USA* **90**, 11014–11018 (1993).
29. Overmeer, R. M. et al. Replication factor C recruits DNA polymerase delta to sites of nucleotide excision repair but is not required for PCNA recruitment. *Mol. Cell Biol.* **30**, 4828–4839 (2010).
30. Hashiguchi, K., Matsumoto, Y. & Yasui, A. Recruitment of DNA repair synthesis machinery to sites of DNA damage/repair in living human cells. *Nucleic Acids Res.* **35**, 2913–2923 (2007).
31. Liu, Y., Deng, Y., Li, G. & Zhao, J. Replication factor C1 (RFC1) is required for double-strand break repair during meiotic homologous recombination in *Arabidopsis*. *Plant J.* **73**, 154–165 (2013).
32. Yao, T., Jin, D., Liu, Q. & Gong, Z. Abscisic acid suppresses the highly occurred somatic homologous recombination in Arabidopsis rfc1 mutant. *J. Genet. Genomics* **40**, 465–471 (2013).
33. Qian, J. et al. Arabidopsis replication factor C4 is critical for DNA replication during the mitotic cell cycle. *Plant J.* **94**, 288–303 (2018).
34. Kani, S. et al. Proneural gene-linked neurogenesis in zebrafish cerebellum. *Dev. Biol.* **343**, 1–17 (2010).
35. Dey, M. R. et al. Granule cells constitute one of the major neuronal subtypes in the molecular layer of the posterior cerebellum. *eNeuro* https://doi.org/10.1523/ENEURO.0289-21.2022 (2022).
36. Laboratory, T. J. Alleles produced for the KOMP project by The Jackson Laboratory. *MGI Direct Data Submission* (2012).
37. Chang, W., Pedroni, A., Koster, R. W., Giacomello, S. & Ampatzis, K. Purkinje cells located in the adult zebrafish valvula cerebelli exhibit variable functional responses. *Sci. Rep.* **11**, 18408 (2021).
38. Pose-Mendez, S., Schramm, P., Valishetti, K. & Koster, R. W. Development, circuitry, and function of the zebrafish cerebellum. *Cell Mol. Life Sci.* **80**, 227 (2023).
39. Raj, B. et al. Emergence of neuronal diversity during vertebrate brain development. *Neuron* **108**, 1058–1074 e1056 (2020).
40. Sur, A. et al. Single-cell analysis of shared signatures and transcriptional diversity during zebrafish development. *Dev. Cell* **58**, 3028–3047 e3012 (2023).
41. Hibi, M. & Shimizu, T. Development of the cerebellum and cerebellar neural circuits. *Dev. Neurobiol.* **72**, 282–301 (2012).
42. Machold, R., Klein, C. & Fishell, G. Genes expressed in Atoh1 neuronal lineages arising from the r1/isthmus rhombic lip. *Gene Expr. Patterns***11**, 349–359 (2011).
43. Kidwell, C. U., Su, C. Y., Hibi, M. & Moens, C. B. Multiple zebrafish atoh1 genes specify a diversity of neuronal types in the zebrafish cerebellum. *Dev. Biol.* **438**, 44–56 (2018).
44. Hoshino, M. et al. Ptf1a, a bHLH transcriptional gene, defines GABAergic neuronal fates in cerebellum. *Neuron* **47**, 201–213 (2005).
45. Seto, Y. et al. Temporal identity transition from Purkinje cell progenitors to GABAergic interneuron progenitors in the cerebellum. *Nat. Commun.* **5**, 3337 (2014).
46. Clark, D. W. et al. NUPR1 interacts with p53, transcriptionally regulates p21 and rescues breast epithelial cells from doxorubicin-induced genotoxic stress. *Curr. Cancer Drug Targets* **8**, 421–430 (2008).
47. Zhao, B. et al. TEAD mediates YAP-dependent gene induction and growth control. *Genes Dev.* **22**, 1962–1971 (2008).
48. Rouault, J. P. et al. Identification of BTG2, an antiproliferative p53-dependent component of the DNA damage cellular response pathway. *Nat. Genet.* **14**, 482–486 (1996).
49. Osman, F. & Whitby, M. C. Emerging roles for centromere-associated proteins in DNA repair and genetic recombination. *Biochem. Soc. Trans.* **41**, 1726–1730 (2013).
50. Sugasawa, K. et al. Xeroderma pigmentosum group C protein complex is the initiator of global genome nucleotide excision repair. *Mol. Cell* **2**, 223–232 (1998).
51. Joo, J. et al. Nucleotide excision repair gene ERCC2 and ERCC5 variants increase risk of uterine cervical cancer. *Cancer Res. Treat.* **48**, 708–714 (2016).
52. Fan, T. et al. The chromatin remodeler ERCC6 and the histone chaperone NAP1 are involved in apurinic/apyrimidinic endonuclease-mediated DNA repair. *Plant Cell* **36**, 2238–2252 (2024).
53. Dueva, R. & Iliakis, G. Replication protein A: a multifunctional protein with roles in DNA replication, repair and beyond. *NAR Cancer* **2**, zcaa022 (2020).
54. Fritsch, M. et al. Caspase-8 is the molecular switch for apoptosis, necroptosis and pyroptosis. *Nature* **575**, 683–687 (2019).
55. Levine, A. J. & Oren, M. The first 30 years of p53: growing ever more complex. *Nat. Rev. Cancer* **9**, 749–758 (2009).
56. Pawlowski, J. & Kraft, A. S. Bax-induced apoptotic cell death. *Proc. Natl Acad. Sci. USA* **97**, 529–531 (2000).
57. Dilla, T., Velasco, J. A., Medina, D. L., Gonzalez-Palacios, J. F. & Santisteban, P. The MDM2 oncoprotein promotes apoptosis in p53-deficient human medullary thyroid carcinoma cells. *Endocrinology* **141**, 420–429 (2000).
58. Sharma, A., Singh, K. & Almasan, A. Histone H2AX phosphorylation: a marker for DNA damage. *Methods Mol. Biol.* **920**, 613–626 (2012).
59. Prabhu, K. S. et al. H2AX: A key player in DNA damage response and a promising target for cancer therapy. *Biomed. Pharmacother.* **175**, 116663 (2024).
60. Solier, S. et al. Heat shock protein 90alpha (HSP90alpha), a substrate and chaperone of DNA-PK necessary for the apoptotic response. *Proc. Natl Acad. Sci. USA* **109**, 12866–12872 (2012).
61. Takashima, H. et al. Mutation of TDP1, encoding a topoisomerase I-dependent DNA damage repair enzyme, in spinocerebellar ataxia with axonal neuropathy. *Nat. Genet.* **32**, 267–272 (2002).
62. O'Connor, E. et al. Mutations in XRCC1 cause cerebellar ataxia and peripheral neuropathy. *J. Neurol. Neurosurg. Psychiatry* **89**, 1230–1232 (2018).
63. Hoch, N. C. et al. XRCC1 mutation is associated with PARP1 hyperactivation and cerebellar ataxia. *Nature* **541**, 87–91 (2017).
64. Rudenskaya, G. E. et al. Ataxia with oculomotor apraxia type 4 with PNKP common "Portuguese" and novel mutations in two Belarusian families. *J. Pediatr. Genet* **8**, 58–62 (2019).
65. Paucar, M. et al. Expanding the ataxia with oculomotor apraxia type 4 phenotype. *Neurol. Genet* **2**, e49 (2016).
66. Magrino, J. et al. A thermosensitive PCNA allele underlies an ataxia-telangiectasia-like disorder. *J. Biol. Chem.* **299**, 104656 (2023).
67. Mahale, R. R. et al. A rare case of ataxia-telangiectasia-like disorder with MRE11 mutation. *J. Pediatr. Neurosci.* **15**, 283–285 (2020).
68. Sedghi, M. et al. Ataxia-telangiectasia-like disorder in a family deficient for MRE11A, caused by a MRE11 variant. *Neurol. Genet.* **4**, e295 (2018).
69. Sandoval, N. et al. Characterization of ATM gene mutations in 66 ataxia telangiectasia families. *Hum. Mol. Genet.* **8**, 69–79 (1999).
70. Shin, U. & Lee, Y. Unraveling DNA repair processes in vivo: insights from zebrafish studies. *Int. J. Mol. Sci.* https://doi.org/10.3390/ijms241713120 (2023).
71. Wang, Y. et al. Structural investigation of pathogenic RFC1 AAGGG pentanucleotide repeats reveals a role of G-quadruplex in dysregulated gene expression in CANVAS. *Nucleic Acids Res.* **52**, 2698–2710 (2024).
72. Ohayon, D. et al. Cytoplasmic proliferating cell nuclear antigen connects glycolysis and cell survival in acute myeloid leukemia. *Sci. Rep.* **6**, 35561 (2016).

73. Tang, D. et al. Cytoplasmic PCNA is located in the actin belt and involved in osteoclast differentiation. *Aging* **12**, 13297–13317 (2020).
74. Thisse, C. & Thisse, B. High-resolution in situ hybridization to whole-mount zebrafish embryos. *Nat. Protoc.* **3**, 59–69 (2008).
75. Zheng, G. X. et al. Massively parallel digital transcriptional profiling of single cells. *Nat. Commun.* **8**, 14049 (2017).
76. Dobin, A. et al. STAR: ultrafast universal RNA-seq aligner. *Bioinformatics* **29**, 15–21 (2013).
77. Martin, F. J. et al. Ensembl 2023. *Nucleic Acids Res.* **51**, D933–D941 (2023).
78. Hao, Y. et al. Dictionary learning for integrative, multimodal and scalable single-cell analysis. *Nat. Biotechnol.* **42**, 293–304 (2024).
79. Jiang, M. et al. Characterization of the zebrafish cell landscape at single-cell resolution. *Front. Cell Dev. Biol.* **9**, 743421 (2021).
80. Hafemeister, C. & Satija, R. Normalization and variance stabilization of single-cell RNA-seq data using regularized negative binomial regression. *Genome Biol.* **20**, 296 (2019).
81. Chung, N. C. & Storey, J. D. Statistical significance of variables driving systematic variation in high-dimensional data. *Bioinformatics* **31**, 545–554 (2015).
82. Lange, M. et al. A multimodal zebrafish developmental atlas reveals the state-transition dynamics of late-vertebrate pluripotent axial progenitors. *Cell* **187**, 6742–6759.e17 (2024).
83. Lin, X., Chau, C., Ma, K., Huang, Y. & Ho, J. W. K. DCATS: differential composition analysis for flexible single-cell experimental designs. *Genome Biol.* **24**, 151 (2023).
84. Bunis, D. G., Andrews, J., Fragiadakis, G. K., Burt, T. D. & Sirota, M. dittoSeq: universal user-friendly single-cell and bulk RNA sequencing visualization toolkit. *Bioinformatics* **36**, 5535–5536 (2021).

Acknowledgements

We thank Pr Masahiko Hibi (Tokyo, Japan) for providing antibodies against pvalb7, neurod1, and vglut1 and associated protocols. We thank Dr Gary Armstrong (McGill University) for the use of the *olig2:GFP* transgenic line. We thank the CRCHUM animal facility, particularly the zebrafish platform, for their help and support in maintaining our fish colonies. We also thank the CRCHUM Cell Imaging Core Facility for access to confocal microscopy (Canadian Innovation Foundation) and particularly Aurélie Cleret-Buhot for her help in image acquisition and analysis. Finally, we thank the IRCM genomic platform for its rigorous work preparing single-cell RNA libraries. This work was funded by the Centre d'excellence en recherche sur les maladies orphelines—Fondation Courtois (CERMO-FC), by Génome Quebec and Ataxie Canada. E.S. and S.A.P. are supported by the Natural Science and Engineering Research Council (NSERC), Canadian Institutes of Health Research (CIHR), and are FRQS research scholars. M.T. is a Junior 2 FRQS research scholar. F.N. received M.Sc scholarships from CRCHUM and the Faculty of Medicine/Université de Montreal. S.A. received doctoral scholarships from CRCHUM, Faculty of Medicine/Université de Montreal, CERMO-FC, FRQS, and CIHR.

Author contributions

Conceptualization, E.S., S.A.P., and F.N.; Methodology: E.S., S.A.P., F.N., A.DSB and M.L; Investigation: F.N., S.A., A.d.S.B., S.T., and C.Z.; Formal analysis and data curation: S.A.; Resources: N.P., M.T., and E.S.; Writing original draft: E.S. and F.N.; Writing—review & editing: S.A.P., N.P., and M.T.; Visualization: N.P., E.S., and S.A.; Supervision: E.S., S.A.P., N.P., and M.T.; Project administration and funding acquisition: E.S.

Competing interests

E.S. is a co-founder of DanioDesign Inc. (QC, Canada) and of Osta Therapeutics (France); N.P. is a co-founder of Neurenati Therapeutics (QC, Canada). These commercial affiliations did not play any role in investigational design, data collection and analysis, the decision to publish or the preparation of the manuscript. The remaining authors declare no competing interests.

Additional information

Supplementary information The online version contains supplementary material available at https://doi.org/10.1038/s41467-025-60775-5.

Correspondence and requests for materials should be addressed to Éric Samarut.

Peer review information *Nature Communications* thanks the anonymous reviewers for their contribution to the peer review of this work. A peer review file is available.